AUTOMOTIVE FMCW RADAR INTERFERENCE ANALYSIS FOR DIFFERENT SCENARIOS

MASTER THESIS REPORT

Yue CHEN

AUTOMOTIVE FMCW RADAR INTERFERENCE ANALYSIS FOR DIFFERENT SCENARIOS

Thesis

to obtain the degree of Master of Science
in Electrical Engineering
at Delft University of Technology
to be defended publicly on 13.04.2023

by

Yue CHEN

Born in Zhejiang Province, China

This thesis has been approved by

Responsible Professor: Prof. DSc. Alexander Yarovoy
Daily Supervisor: Dr. Utku Kumbul

Thesis committee:

Prof. DSc. Alexander Yarovoy,	Technische Universiteit Delft
Dr. Nitin Myers,	Technische Universiteit Delft
Dr. Utku Kumbul,	Technische Universiteit Delft

Keywords: Automotive Radar, FMCW Radar, Mutual interference, Performance analysis

An electronic version of this dissertation is available at
http://repository.tudelft.nl/.

ACKNOWLEDGEMENTS

First, I would like to express my gratitude to the Microwave Sensing, Signals and Systems (MS3) Group for giving me the opportunity to end my master program with an amazing topic.

I appreciate all the guidance and large amount of valuable time from my supervisors, Prof. Alexander Yarovoy and Utku Kumbul. They put a lot of effort into helping me through the entire thesis. They are always patient whenever I have any questions and gave me a lot of insightful expertise to help me push further.

My sincere thanks extend to MSc students in the MS3 Group and all my friends, their accompany through the Covid period means quite a lot to me.

In the end, the support of my family should be emphasized. Without them, I would have no chance to study abroad and explore the world. Although we have not met each other for 2 years, they were encouraging me all the time. I hope we could have a reunion in the near future.

My master comes to an end, but another new journey has just begun. Again, thank you to everyone who has supported me.

ABSTRACT

Nowadays, automotive industry is developing rapidly and autonomous driving gains lots of attention. Automotive radars play a crucial role due to its advantages of weather tolerance and ability of detecting targets under occlusion. In the near future, a large number of automotive radars will be on the road which leads to the problem of mutual interference among radars. Thus, it is important to understand the characteristic and impact of the interference. Since Frequency Modulated Continuous Wave (FMCW) radars are the most commonly used radar in the automotive industry, FMCW-to-FMCW mutual interference is a necessary topic to study.

Previous work related to the analytical signal model of FMCW-to-FMCW mutual interference usually stops before Two-dimensional (2D-FFT). The mathematical model for mutual interference after 2D-FFT in the range-Doppler domain remains empty. Furthermore, the performance analysis related to the probability of detection and the probability of false alarm with different Signal-to-interference Ratio (SIR) is also absent.

To fill these gaps, we proposed to derive and validate the analytical model for FMCW-to-FMCW mutual interference in an ideal situation and analysis the performance on the probability of detection and the probability of false alarm. The interference behaves differently depending on the chirp bandwidth and duration. Therefore, according to the relationship between victim signal's and interference signal's chirp bandwidth and duration, we classified all the situation into four cases, fully synchronous, general synchronous, periodic asynchronous, and aperiodic asynchronous. In this thesis the mathematical model of the first three cases are derived and validated.

Constant False Alarm Rate (CFAR) detection is applied to analyze the relation among SIR, the probability of detection P_d and the probability of false alarm P_{FA} in this thesis. In the fully synchronous case, the interference formed as a ghost target after processing. SIR at the input of the receiver will not have a significant impact on the probability of detection. The generally synchronous interference tends to be concentrated in one velocity profile. When the value of velocity is close to the victim signal's, P_d will be increased with higher SIR. Asynchronous interference is randomly distributed on the range-Doppler map after processing. Similar to generally synchronous interference, a higher SIR can lead to a higher P_d. In all cases, the trend-off between P_d and P_{FA} exists. The lower desired P_{FA}, a higher P_d can be achieved.

CONTENTS

LIST OF FIGURES

LIST OF TABLES

ABBREVIATIONS

2D-FFT Two-dimensional. vi, 9, 15, 18, 19, 32, 35, 40, 41, 44

ADAS Advanced Driver-assistance System. 1–3, 50

ADC Analog-to-Digital Converter. 6

CFAR Constant False Alarm Rate. vi, 4, 9, 15, 16, 19, 38–42, 44, 45, 47–50

CPI Coherent Processing Interval. 14, 26

CW Continuous Wave. 2

FFT Fast Fourier Transform. 7–10, 18, 30, 33, 35

FMCW Frequency Modulated Continuous Wave. vi, 1–11, 19, 27, 32, 35, 37, 49–51

IF Intermediate Frequency. 6, 7

PC-FMCW Phase Coded-Frequency Modulated Continuous Wave. 2, 51

PMCW Phase Modulated Continuous Wave. 2

RCS Radar Cross Section. 12, 17

ROC Receiver Operating Characteristic. 38, 41, 43, 45, 46, 48–51

SIR Signal-to-interference Ratio. vi, 3, 32, 35–38, 40–43, 45, 46, 48–51

SNR Signal-to-noise Ratio. 3, 15, 16, 19, 51

VCO Voltage-controlled Oscillator. 8, 10, 11

1

INTRODUCTION

In this chapter, the background of FMCW automotive radar is described in Section 1.1 first. Based on that, motivation has emerged. The next section describes the procedure for formulating the research problem, including finding the research gap and illustrating the research problem of this thesis. Finally, Section 1.4 gives the structure of the remaining chapters of this thesis.

1.1. BACKGROUND

As the automotive industry develops, autonomous driving becomes the trend and the focus of society [1][2][3]. To achieve high-level autonomous driving, Advanced Driver-assistance System (ADAS) is one of the crucial parts of technology [4]. According to [5], more than 90% of traffic accidents are caused by human factors of negligence. As shown in Figure 1.1, the applications of ADAS include adaptive cruise control, cross-traffic alert, and blind spot detection that help drivers understand the driving situation and avoid traffic accidents [6]. To realize these applications, radar is widely used for range estimation, velocity estimation, and angle estimation to detect obstacles or other vehicles on the road.

1

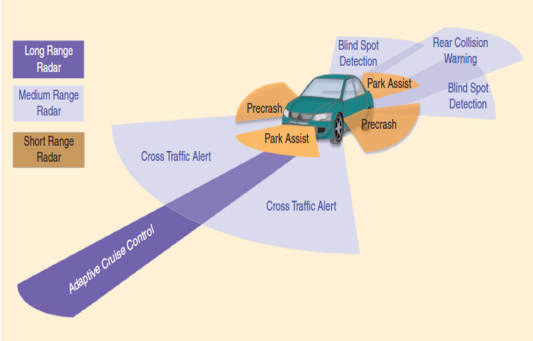

Figure 1.1: ADAS consists of different range radars [1]

Compared to video cameras or lasers, automotive radar exploits the reflections of electromagnetic waves, making the radar capable of working in bad visual conditions,i.e., snowing, flogging, or in darkness [7]. With the progress of semiconductor technology in millimeter waves, automotive radars play an important role in the detection of objects in ADAS.

For automotive radar applications, there are various waveforms, namely Continuous Wave (CW), FMCW, Phase Modulated Continuous Wave (PMCW) and Phase Coded-Frequency Modulated Continuous Wave (PC-FMCW). The PC-FMCW radar is new to the industry, and the realization of such a waveform is an ongoing research topic [8–14]. Currently, FMCW is the most common waveform in the automotive industry [15][16]. However, the FMCW radars are weak against radar-to-radar interference [4, 17–19].

With the rapid growth of autonomous driving, the number of radars in cars is increasing. One of the foreseeable future automotive radar working conditions is driving on a busy city road, and all the cars are equipped with multiple automotive radars. As a consequence, safety concerns about radar-to-radar interference are raised [8][10]. A large amount of interference, to some extent, could cause false alarms or miss detection in ADAS, leading to drivers making wrong decisions and causing traffic accidents.

Based on the background information above, **motivation** for this thesis is revealed:

- **To understand the characteristics and impact of the interference better, analytical investigation of FMCW radar-to-radar interference is needed.**

1.2. PROBLEM FORMULATION

After reviewing the literature on FMCW interference research, it is found that mutual interference between radars depends on interference radar waveform type and parameters [8–10, 20, 21]. Referring to [10], it gives the mathematical expression of the output before the range profile in the time domain. It contains mutual interference between different waveforms, including CW, FMCW, PMCW and PC-FMCW. With these well-established mathematical expressions about mutual interference between various types of the waveform, other researchers can investigate the interference impact much easier. However,

in most cases, the final results of automotive radar detection are interested in the range-Doppler domain, which contains range and velocity information. Therefore, the idea of investing the mathematical model in the range-Doppler domain has emerged. As mentioned above, FMCW radar is now the most widely used radar, starting the investigation of the derivation from FMCW-to-FMCW is an appropriate choice.

On the other hand, there are few performance analyses about the relationship among the probability of detection, the probability of false alarm, and SIR. In [22], it shows the probability of detection over the different SIR. In [23], the impact of distance on the probability of a false alarm is given. The related papers mentioned one or two factors in the performance analysis part, nevertheless, the analysis that encompasses all three factors of FMCW-to-FMCW mutual interference is currently incomplete or missing.

Summarizing the problem formulation process above, there are two main gaps based on the literature so far:

- The mathematical model for FMCW-to-FMCW mutual interference in the range-Doppler domain is absent.
- Performance analysis of the relationship among the probability of detection, the probability of false alarm, and SIR is not there.

The research problem is formulated with reference to these gaps:

'What is the analytical signal model for FMCW-to-FMCW mutual interference in the range-Doppler domain? And how does the SIR or Signal-to-noise Ratio (SNR) affect the probability of detection and the probability of false alarm? '

1.3. RESEARCH CONTRIBUTIONS

The main research contributions of this thesis are concluded as follows:

- Derive the analytical model for FMCW mutual interference in range-Doppler domain for different cases. The model is also verified by comparing the numerical simulations of the equations with the quantitative simulation. The analytical model provides convenience for researchers studying FMCW-to-FMCW mutual interference. They could easily set up simulations of the various interference cases by entering the basic parameters, i.e. bandwidth, chirp duration, and range, with the model we derived to observe the interference behavior.
- The results of the performance analysis for FMCW-to-FMCW mutual interference in different cases with respect to the probability of detection, the probability of false alarm and SIR to give a vision of how interference will affect the accuracy of the detection and sensing the objects. This is important in the application of ADAS to ensure the safety of drivers.

1.4. THESIS OUTLINE

The remaining chapters of this thesis are structured as follows. Chapter 2 briefly introduced the basic knowledge of FMCW radar, including the strength, the architecture of

the system, and the simplified signal models of the typical processing procedure. Chapter 3 is based on the signal models mentioned in Chapter 2. It introduces the algorithm to perform the processing of FMCW radar signal for simulation and shows how the signal behaves in the time and frequency domains after each step. Chapter 4 presents the derivation and verification of the quantitative simulation of the analytical expression of FMCW-to-FMCW mutual interference in the range-Doppler domain. In this chapter, mutual interference is divided into 2 different types: synchronous and asynchronous. Chapter 5 contains the algorithm and results of the performance analysis of the different cases of mutual interference by applying the detection method CFAR. The last chapter, Chapter 6, draws conclusions from this thesis and provides suggestions for future work.

2

FUNDAMENTALS OF FMCW RADAR

In this chapter, the basic knowledge of FMCW Radar is presented. In Section 2.1, a brief history of the development of the FMCW radar and the strength of FMCW radar in the automotive industry is introduced. Next, the FMCW radar architecture is given and it is shown the general working principle of the FMCW radar system. In the end, the signal model is presented to describe the working process analytically.

Currently, the most widely used automotive radar system is the FMCW radar [15][16]. It is a radar whose transmitted signal is a sinusoidal signal with periodic chirps. In every single chirp, the signal frequency changes linearly over time [16][23]. Figure 2.1 shows the classic FMCW transmitted signal and the received signal in one single chirp. During one chirp duration T, the frequency of the signal increases the amount of bandwidth B. Between the received signal and the transmitted signal, there is a time delay, marked τ, which creates the frequency difference on the received signal at that time. The difference in frequency provides information on the range of objects [24]. To obtain velocity information, multiple chirps are sent continuously, creating Doppler frequency shifts. Details will be presented in Section 2.3.

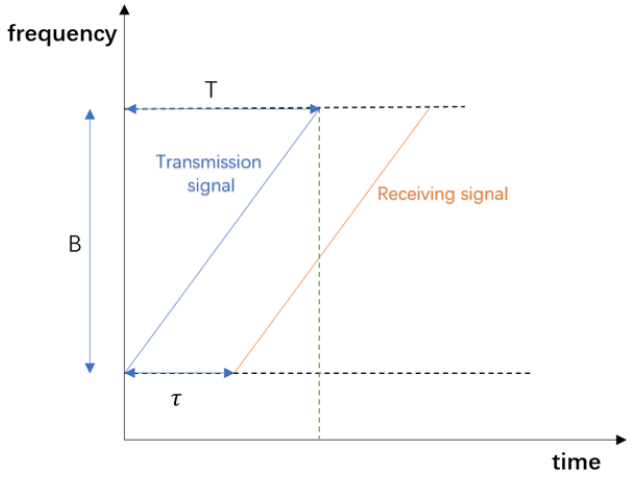

Figure 2.1: FMCW transmitted signal and received signal in a single chirp

2.1. STRENGTHS

At first, the FMCW radar is applied only to military use, such as proximity fuzes for artillery projectiles. It has features of small size, low cost, excellent reliability and freedom from jamming. These are huge advantages on the battlefield [25]. Due to the nature of the military, articles and information about FMCW radar are not published. Its widespread industrial application started in the 1980s. In the 1980s, FMCW radar was primarily used in the automotive industry for collision avoidance systems, distance measurement, and speed detection. The technology was also used in the aviation industry for altitude and range measurement [26]. Compared to other types of radar, the three main strengths of the FMCW radar are listed below [27]:

- *Compression of the signal bandwidth when transferring RF signal to IF signal* In a FMCW radar system, the Intermediate Frequency (IF) signal or beat frequency signal received after mixing is characterized by a frequency equal to the difference between the current transmission frequency and the current reception frequency of the chirp. This feature leads to a maximum frequency of the beat signals equivalent to twice the product of the chirp slope and the two-way propagation distance to the target. The maximum frequency corresponds to the bandwidth of the beat frequency signals, which is significantly smaller compared to the IF signal bandwidth in other radar systems. By decreasing the bandwidth of the IF signal, the Analog-to-Digital Converter (ADC) sampling frequency required for the signal processing can be substantially reduced. This reduction in the sampling frequency results in simplification of the digital processing chain, thereby decreasing the computational power requirements and physical memory utilization, ultimately resulting in a simpler, more efficient, and cost-effective radar system.

- *Low power consumption*

FMCW radar is a type of radar that continuously transmits a frequency-modulated signal as a continuous wave. Unlike pulsed radar, there is no need for the transmitter to be idle during operation. The transmitter emits a signal that varies in frequency over time, while the receiver listens for the signal that is reflected from targets in the environment. Compared to pulsed radar, which requires short, high-power pulses of RF energy and periods of idleness between pulses, FMCW radar eliminates the need for high-power pulses. This is because the transmitted power is spread out over a longer period of time, resulting in lower average power consumption.

Due to the low power requirements, FMCW radar systems are well-suited for applications where power consumption is a concern, such as in mobile or battery-operated devices. They also have the advantage of being able to detect objects at close ranges with high resolution, which can be difficult for pulsed radar systems due to the need for high peak power to overcome noise and interference.

- *Compact size*

  Compared to other types of radar, FMCW radar has a smaller size due to its narrower IF bandwidth and low power consumption, as mentioned earlier. The low power requirements, enables the use of smaller low-power components, which can be easily integrated into the radar system. Additionally, the reduced complexity of processing components resulting from the narrow bandwidth of the digital signals leads to a reduction in the overall size of the radar system.

2.2. RADAR SYSTEM ARCHITECTURE

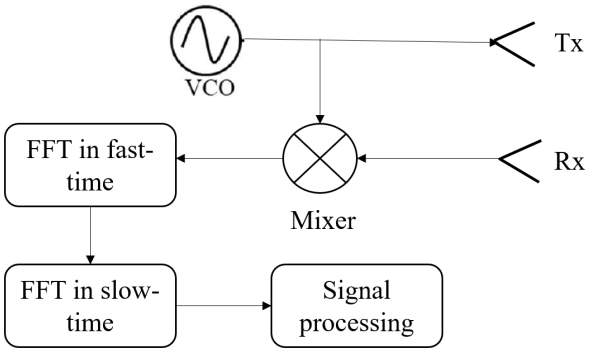

Figure 2.2: Simplified FMCW radar system architecture block diagram

A simplified block diagram of the FMCW radar architecture is presented in Figure 2.2. The entire system is formulated by six parts: signal generation, transmission and receiving, dechirping, Fast Fourier Transform (FFT) in fast-time, FFT in slow-time, and signal processing [22].

- *Signal generation*

  Voltage-controlled Oscillator (VCO) is an electronic oscillator that is capable of generating signals whose frequency is determined by the input voltages applied to it. VCOs are commonly used to produce chirp signals [28]. Over the period from 2001 to 2006, advancements in silicon fabrication technology led to a significant increase in the maximum operating frequency of VCOs, from 25.9 GHz to 117.2 GHz [29][30]. This makes VCOs a suitable source for generating FMCW signals for automotive radar applications.

  The VCO continuously generates FMCW signals with predetermined bandwidth, chirp duration, and carrier frequency. The output signal is then transmitted to two components: the transmission antenna and the mixer. By utilizing VCOs as waveform generation sources, FMCW radar systems can be effectively implemented in automotive applications [31].

- *Transmission and receiving*

  The signal produced by the oscillator is subjected to amplification at the transmitter and is then transmitted toward the intended target. The signal subsequently gets reflected back from the objects in the target's vicinity, and the resulting echo is captured by the radar receiver. The received signal is then amplified at the receiver and directed toward the mixer for further processing. This process of signal transmission and reception enables the effective operation of radar systems for a variety of applications.

- *Dechirping*

  The input of dechirping includes two parts: the transmitted signal and the received signal. In the mixer, the received signal is multiplied by the conjugate of the transmitted signal (without transmission power). In this way, the beat signal at the intermediate frequency is obtained [23]. If there is any interference signal, the captured interference might spread over the frequency domain after dechirping. This is because the frequency difference of most signals is constantly changing and the relative beat frequency will not be constant. This step gives FMCW the advantages of high resolution and low transmission power.

- *FFT in fast-time*

  The first FFT in fast time converts the output of the mixer from the time domain to the frequency domain. In addition, the range profile can be computed by

$$R = \frac{f_b c}{2k} \tag{2.1}$$

  where R is the range, f_b is the beat frequency of the signal, c is the speed of light, and $k = \frac{B}{T}$ is the sweep slope.

- *FFT in slow-time*

  The next step is to obtain the Doppler frequency by applying the second FFT in slow time to the result of FFT in fast time. The slow time here indicates the profile

of the number of chirps. The velocity profile can be converted from Doppler shifts by

$$v = \frac{\lambda f_d}{2} \tag{2.2}$$

where v is velocity, λ is the wavelength, f_d denotes the Doppler frequency. After applying FFT in both fast and slow time, the range-Doppler map is formulated.

- *Signal processing*

  The last step is signal processing, which mainly includes detection and classification. For radar target detection, CFAR is one of the most popular algorithms [32][33]. And for classification, Machine Learning or Deep learning is the focus of research in the industry today [34][35].

2.3. SIGNAL MODEL

The frequency of FMCW signal normally starts from the carrier frequency f_c and increases or decreases linearly over time by the chirp slope k. The transmitted signal $s(t)$ can be written as

$$s(t) = \sqrt{P_t} e^{-2j\pi(f_c t + \frac{kt^2}{2})} \tag{2.3}$$

Here P_t is the transmission power. This equation presents the transmitted signal in the first chirp. Therefore, when multiple chirps are mentioned, t from Equation 2.3 is defined as $nT + t'$, t' as the time from the start of the nth chirp. Then, Equation 2.3 becomes:

$$s(n, t') = \sqrt{P_t} e^{-2j\pi(f_c(nT+t') + \frac{k(nT+t')^2}{2})} \tag{2.4}$$

The transmitted signal is reflected by the object and is received by the receiver after the round-trip time delay τ. The received signal can be expressed as $s_r(t)$.

$$s_r(n, t') = \sqrt{P_r} e^{-2j\pi(f_c(nT+t'-\tau) + \frac{k(nT+t'-\tau)^2}{2})} \tag{2.5}$$

where P_r is the power of the signal after attenuation of propagation and amplification at the receiver. Referring to the procedure in Section 2.2, the next step is dechirping. The received signal multiplies with the conjugate of the transmitted signal at the mixer, which is described as:

$$\begin{aligned} s_m(t) &= s_r(t) e^{2j\pi(f_c t + \frac{k}{2} t^2)} \\ &= \sqrt{P_r} e^{2j\pi(k\tau t + f_c \tau - \frac{k\tau^2}{2})} \end{aligned} \tag{2.6}$$

For simplification, the time parameter here is denoted as t. From Equation 2.6, we can find that $k\tau$ influences the signal over time, which is called beat frequency. The beat frequency indicates the difference in frequency between the transmitted signal and the received signal. Since $\tau = \frac{2(R+v(nT+t'))}{c}$ is also related to the range of the object and the relative velocity, the range and velocity information can be obtained from the beat frequency. For the derivation of the beat frequency, 2D-FFT is applied. The first FFT is applied over every chirp over time samples, and the range profile is achieved by converting the beat frequency through Equation 2.1. Meanwhile, the beat frequency resolution

Δf_b can be found by exploiting the radar range resolution ΔR that describes the minimum range in which two targets can be distinguished. To avoid the absence of frequency information, Δf_b must be consistently smaller than the frequency $\frac{1}{T}$ [36][37]. The resolution of the range can be obtained by 2.7.

$$\Delta R = \frac{c}{2B} \tag{2.7}$$

$$\Delta f_b = \frac{2B\Delta R}{cT} \tag{2.8}$$

The resolution of the beat frequency is based on the range resolution. The second FFT in slow time is based on the term $\frac{2f_c vnT}{c}$. The beat frequency changes with respect to the consequent number of chirps. This is the Doppler frequency shift $\frac{2f_c v}{c}$, which can be derived by applying the FFT over the number of chirps. Similarly, the velocity resolution can be computed:

$$\Delta v = \frac{1}{2\lambda nT} \tag{2.9}$$

After 2D-FFT processing, the range-Doppler map in range and velocity profile is acquired.

2.4. CONCLUSION

In this chapter, the basic knowledge of FMCW radar is presented. FMCW shows the advantages of compression of the signal bandwidth, low power consumption and compact size in the military. These strengths attracted the automotive industry. In particular, FMCW radar has a high resolution, reliability at dynamic ambient temperature and quick updating of measurements, making FMCW radar the main automotive radar for object detection.

The architecture of the system FMCW consists of signal generation (in VCO), transmission and receiving (using transmitter and receiver), dechirping (in the mixer), FFT in fast-time, FFT in slow-time and signal processing. The signal models of FMCW are obtained without interference or noise. The resulting beat frequency and the Doppler frequency from the multiple chirps give the range and velocity information of the target, respectively.

3

ALGORITHM AND REALIZATION OF FMCW RADAR

To understand how the signal of FMCW radar works intuitively, the simulation results are obtained based on the theory demonstrated in Chapter 2. In this chapter, the simulation process and results of FMCW radar from transmitting the signal to obtain the range-Doppler map are presented. The simulation is based on the ideal situation, which means that there is no interference or noise to influence the target signal. The simulation works in Matlab.

3.1. TRANSMITTED AND RECEIVED RF SIGNAL

The simulation starts with generating the transmitted signal. In this simulation, the output of VCO is a sweep signal with a carrier frequency f_c=77 GHz, a chirp duration T = 25.6 μs and bandwidth B=300 MHz. According to the sampling theorem, the sampling frequency f_s must be twice the maximum of the signal. This means that if the sweep starts with a frequency of 77 GHz, f_s should be at least $2(f_c - B)$ = 153.4 GHz (when the chirp decreases in frequency over time). To reduce the computational load, half the bandwidth $\frac{B}{2}$ is taken as the starting frequency. Thus, the requirement of f_s decreased to 2B = 600 MHz. In this thesis, 1 GHz is set as the sampling frequency. Based on the signal model in Section 2.3, as shown in Figure 3.1, the transmitted signal frequency starts at the frequency of 150 MHz and the frequency linearly decreases to -150 MHz in one chirp duration with the chirp rate $k = \frac{B}{T} = 1.17 \times 10^{13}$ Hz/s.

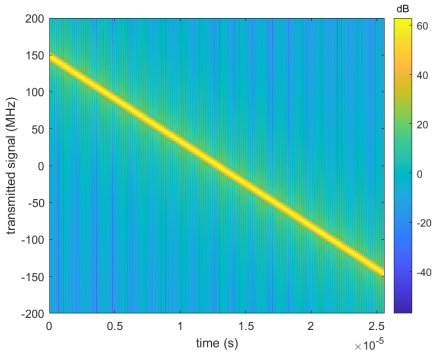

Figure 3.1: The transmitted signal spectrum

At the transmitter, the transmitted power P_t = 30 dB and the gain of the transmitter antenna G_t = 30 dB are brought to the signal. On the other hand, in the receiver, the gain of the received antenna G_r=20 dB.

The target is at a distance R_{target}=50 m while moving at a relative velocity V_{target}=20 m/s. As explained in Section 2.3, the time delay of the received signal is τ=0.336 μs. Figure 3.2 presents that the received signal is received 0.336 μs after starting to send the transmitted signal. The frequency changes the same as the transmitted signal.

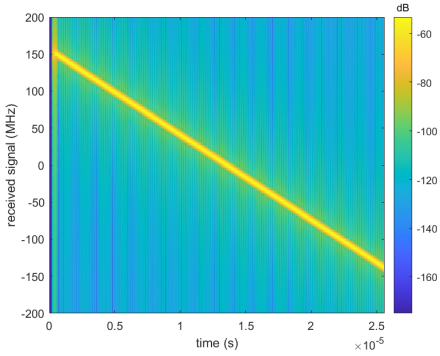

Figure 3.2: The received signal spectrum

The amplitude levels of transmitted and received signal are different as a result of propagation attenuation and the antenna gain of the transmitter and receiver. According to the radar equation, received signal power P_r can be written as

$$P_r = \frac{P_t G_t G_r \lambda^2 \sigma}{(4\pi)^3 R_{target}^4} \tag{3.1}$$

where σ is the target's Radar Cross Section (RCS) equal to 30 dB, and the amplitude level after the receiver should be -104.13 dB. As shown in Figure 3.3, the amplitude of the

received signal is approximately 6.21×10^{-6} which is -104.14 dB, close to the theoretical value.

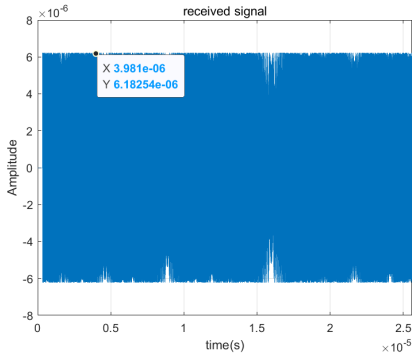

Figure 3.3: The received signal in time domain

All the input parameters mentioned above are listed in Table 3.1.

Parameter	Value
B	300 MHz
T	25.6 μs
f_c	77 GHz
f_s	1 GHz
G_t	30 dB
G_r	20 dB
P_t	30 dB
R_{target}	50 m
V_{target}	20 m/s

Table 3.1: FMCW signal model parameters

3.2. DECHIPRING SIGNAL

The received signal is dechirped in the mixer to obtain the beat frequency. Figure 3.4 shows the beat frequency of the signal after mixer [8][9]. It is located around 3.9 MHz at all times, indicating that the frequency difference between the transmitted signal and the received signal is constant. According to the theory in Chapter 2, the range is $\frac{f_b c}{2k}$ = 49.92 m, which is an approach to the ideal value 50 m.

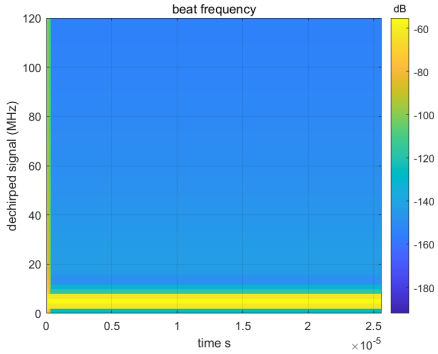

Figure 3.4: The beat frequency after dechirping

3.3. RANGE-DOPPLER

Fast FFT is first applied to derive the value of the beat frequency numerically. To avoid the absence of frequency information, N=131072, where N is the frequency (range) cells used, which is more than twice the signal length. The result is presented in Figure 3.5a. From the figure, it is found that there is a spike that represents the target located at the frequency of 3.918 MHz with -104.243 dB amplitude. If it is transferred to the range profile, as indicated in Figure 3.5b, the target is at a distance of 50.125 m.

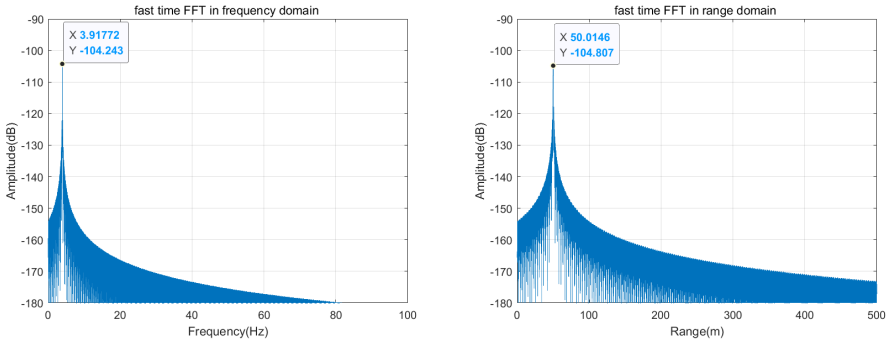

(a) FFT in fast time result in frequency profile (b) FFT in fast time result in range profile

Figure 3.5: Fast FFT results

The simulation above is only for the case of sending one chirp. To investigate the velocity information, 128 chirps are sent in Coherent Processing Interval (CPI) of this simulation. By applying FFT over the number of chirps (slow time) with the amount of velocity bins being 4 times the number of chirps, range-Doppler map is given in Figure 3.6. The cells that contain the most power are presenting the target. In this range-Doppler map, the cells are at a velocity of around 20 m/s and a range of approximately 50 m have the highest power level, which indicates that the detected object is 50 m far away and it

is moving 20 m/s relative to the radar. The value of the distance and velocity information gathered from the simulation is very close to the given parameters. Certainly, the results still have few deviations due to sampling, but it is acceptable.

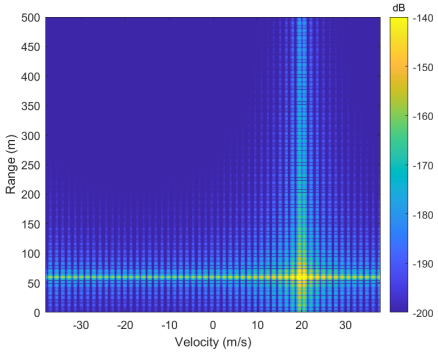

Figure 3.6: The range-Doppler map

3.4. PERFORMANCE

For investigating the performance of the probability of detection with different SNR, CFAR is applied (the details about the method will be introduced in Chapter 5). To have a clearer vision, the level of amplitude of the transmitted signal at the receiver is set as a constant, s=1, and the noise is taken as a parameter to obtain different SNR from -57 dB to -27 dB. Therefore, the corresponding input of the noise amplitude, n, can be calculated by the following:

$$SNR = \frac{s^2}{n^2} \tag{3.2}$$

where the signal and noise power correspond to the values before taking 2D-FFT. Other parameters remain the same as in the previous steps. Figure 3.7 shows the Doppler range results for the interference-free case. This result is used as the input of the CFAR detector. The target spike is located at 50 m with a velocity of 20 m/s. After 2D-FFT, the target spike has an amplitude of around 38.85 dB and the noise floor is about 20 dB with the corresponding input target and noise amplitude is 0 and 59.98 dB, respectively. Thus, SNR computed by applying Equation 3.2, SNR= -26.98 dB.

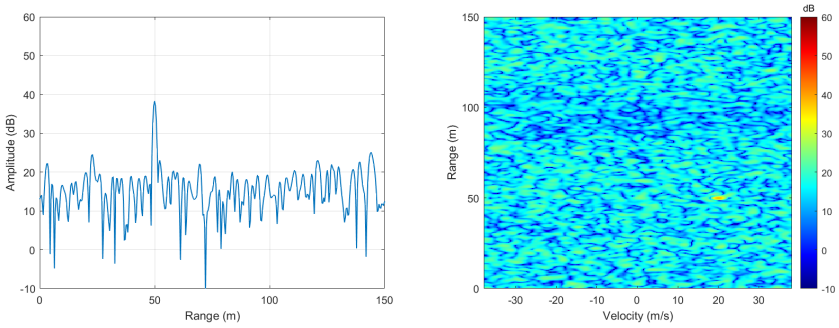

(a) Interference-free case's input in range domain

(b) Interference-free case's input in range-Doppler domain

Figure 3.7: 2D input of interference-free case

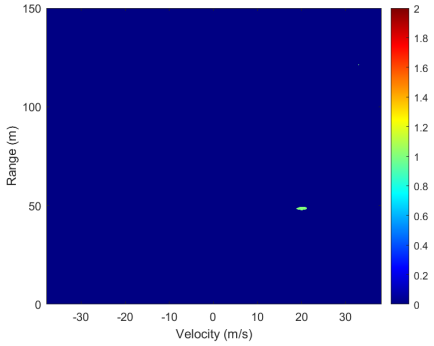

Figure 3.8: CFAR results of interference-free case

By giving the false alarm rates P_{FA}= 10^{-6}, 10^{-5},10^{-4},10^{-3}, and 10^{-2}, the CFAR detector will set the threshold. The higher P_{FA} causes a lower amplitude threshold. Figure 3.8 shows the CFAR result with P_{FA}=10^{-6} when SNR=-26.98 dB. In the figure, there are some cells around the given target location that have a higher amplitude than the threshold and are marked as 1.

The detection setting for the interference-free case is based on giving the corresponding noise power to obtain SNR from -57 dB to -27 dB. Then each SNR will be detected by 5 different P_{FA} which have been listed above. Figure 3.9 illustrates that P_d generally increases with the improvement of SNR. However, there is a trade-off between P_d and P_{FA}. When P_{FA}=10^{-6}, SNR has to be higher than -35 dB to approach P_d = 1. With a higher false alarm rate P_{FA}=10^{-2}, P_d starts to reach 1 since SNR=-39 dB.

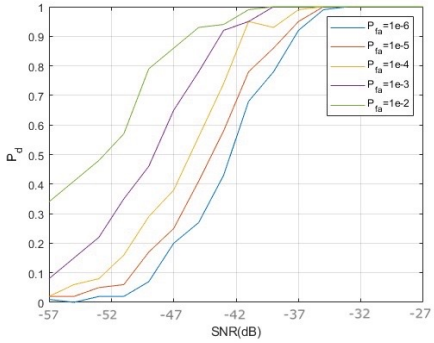

Figure 3.9: The ROC curves of interference-free case

3.5. MULTIPLE TARGETS

In reality, there is normally more than one car and also other obstacles. Let us assume that there are 3 other targets surrounding with different ranges and velocities, which are listed in Table 3.2. For comparison, RCS of three targets are kept the same. Three different targets cause three reflected signals that are summed up at the receiver and sent to the mixer together. Figure 3.10 shows the spectrum of three total dechirped signals. It is seen that there are 3 constant beat frequencies, 8.02 MHz, 23.46 MHz and 39.12 MHz. Based on $\frac{f_b c}{2k}$, the corresponding ranges are 102.58 m, 300.08 m and 500.39 m. The calculated results are close to the ranges in Table 3.2.
Moreover, the three beat frequencies start at various times. This is the consequence of having different distances, the time delays, respectively, are $\tau 1 = 0.70$ μs, $\tau 2 = 2.06$ μs and $\tau 3 = 3.44$ μs for Target1, Target2 and Target3, respectively.

Target	**Range(m)**	**Velocity(m/s)**
Target1	100	10
Target2	300	20
Target3	500	30

Table 3.2: Ranges and velocities of multiple targets

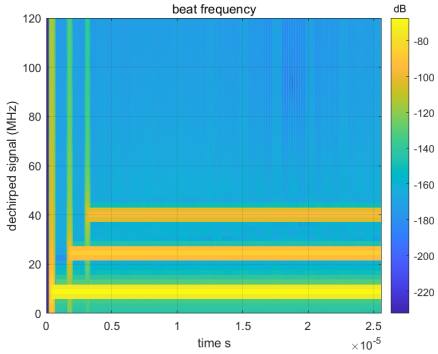

Figure 3.10: The beat frequency of multiple targets after dechirping

After dechirping the received signals, as Figure 3.11 shown, the signals are presented in the frequency domain and converted to the range profile. Three spikes represent the three targets with amplitude of -116.522 dB, -136.033 dB and -145.747dB. According to Equation 3.1, the levels of the amplitude of targets 1, 2 and 3 should be -116.17 dB, -135.25 dB and -144.13 dB which are approaching the simulation values. When we look at the range profile, Figure 3.11b, the locations of the spikes are 100.078 m, 300.039 m and 499.999 m.

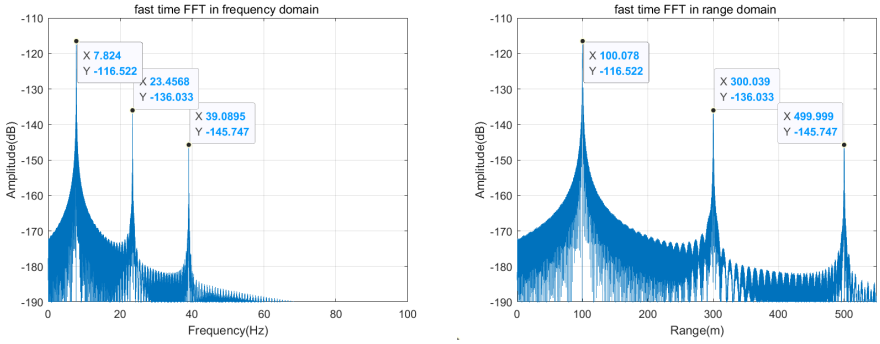

(a) FFT result in fast time in frequency profile of multiple targets

(b) FFT result in fast time in range profile of multiple targets

Figure 3.11: FFT in fast time results of multiple targets

The next is to apply FFT in slow time. The results of 2D-FFT of multiple targets are presented in Figure 3.12. The three cells that contain the highest power in the range-Doppler map are located at around 100 m with 10 m/s velocity, 300 m with 20 m/s velocity, and 500 m with 30 m/s velocity. The results match the parameters given by Table 3.2.

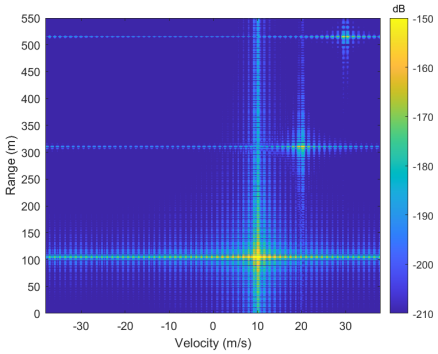

Figure 3.12: The range-Doppler map of multiple targets

3.6. CONCLUSION

The simplified simulation and its results for the FMCW radar signal process, based on Chapter 2, are presented in this chapter. By dechirping the signal, the beat frequency is derived and it is achievable to obtain the information on range and velocity by applying 2D-FFT. The results in range-Doppler map are convincing after comparing it with the theoretical value. According to the CFAR result, higher SNR leads to better performance in the probability of detection aspect. The scenario of multiple targets with different distances and relative speeds is also simulated. In the simulation, all targets are located in the matched position of the range-Doppler map.

In practice, there are more steps or factors, for example, noise from the environment and the devices, applying a windowing function to the dechirped signal before processing to reduce the sidelobe levels.

4

Analytical Analysis of the Interference

In this chapter, the derivation of mathematical expression of FMCW-to-FMCW mutual interference in range-Doppler domain is presented in Section 4.1. Then, the equations derived from Section 4.1 are examined in Section 4.2 by different interference scenarios. In addition, interference behavior is also investigated.

4.1. Mathematical Expression Derivation for FMCW-to-FMCW Interference

In this section, the interference research situation and the signal model are first described in detail. Next, the signal processing of the FMCW radar signal with interference is illustrated theoretically, including signal dechirping, Fourier transform in fast time and slow time. In the end, the mathematical expression of the received signal is derived in the range-Doppler domain.

4.1.1. THE SIGNAL MODEL

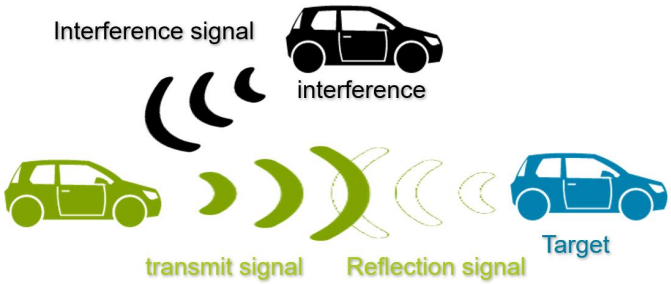

Figure 4.1: Signals propagation model

To estimate the distance between the target car and itself, the FMCW automotive radar in the objective car transmits the FMCW signal $s(t)$ with the transmit power P_t. The transmit signal can be expressed as follows:

$$s(t) = \sqrt{P_t} e^{-2j\pi(f_c t + \frac{kt^2}{2})} \tag{4.1}$$

Here, f_c is the carrier frequency. k is the frequency slope defined by $k = B/T$. B and T are the bandwidth and the chirp duration of the signal, respectively. As shown in Figure. 4.1, the transmit signal $s(t)$ is reflected by the target car and received by the receiver in the objective car. Compared to the transmit signal, the reflection signal in the receiver $s_{rt}(t)$ has a time delay τ and power attenuation due to propagation. Assuming that the signal is propagated in free space, the power of the reflection signal at the receiver is given by the radar equation:

$$P_{tr} = \frac{P_t G_t G_r \lambda^2 \sigma}{(4\pi)^3 R_{target}^4} \tag{4.2}$$

where G_t and G_r refer to the transmission and receiving antenna gain of the radar, λ notes the wavelength of the signal, σ defines the radar cross section (RCS) of the target car, and the distance between the objective car and the target is R_{target} [7]. Since the travel time of the signal is relatively short, the displacement of targets during the propagation is negligible. It can be assumed that the signal propagates at the same distance back and forth. Combined with the power attenuation Equation 4.2 and Equation 4.1 with time delay τ, the reflection signal in the receiver can be mathematically represented as

$$s_{tr}(t) = \sqrt{P_{tr}} e^{-2j\pi(f_c(t-\tau) + \frac{k(t-\tau)^2}{2})} \tag{4.3}$$

Here $\tau = 2R_{target}/c$, where c is the speed of light. Meanwhile, the receiver is highly likely to receive an interfered FMCW signal $s_{int}(t)$ from another car, with transmission power

P_{int}, carrier frequency f_{intc} and chirp frequency slope k_{int}.

$$s_{int}(t) = \sqrt{P_{int}} e^{-2j\pi(f_{intc}t + \frac{k_{int}t^2}{2})} \tag{4.4}$$

The interference car sends the signal at a distance of R_{int} to the victim radar. Similarly to $s(t)$, the power of the interference signal is also attenuated, and there is a delay τ_{int} with respect to R_{int}. The interference signal is transmitted directly to the receiver, propagated only in one way of R_{int}, therefore $\tau_{int} = R_{int}/c$. Regarding the power attenuation of the interference signal, according to the Friis equation, the interference signal power in the receiver can be obtained by

$$P_{ir} = \frac{P_{int} G_{tint} G_r \lambda_{int}^2}{(4\pi)^2 R_{int}^2} \tag{4.5}$$

Here G_{tint} is the gain of the antenna from the interference car and λ_{int} is the wavelength of the interference signal. Taking into account τ_{int}, consequently, the interference signal at the receiver can be expressed as

$$s_{rint}(t) = \sqrt{P_{ir}} e^{-2j\pi(f_{intc}(t-\tau_{int}) + \frac{k_{int}(t-\tau_{int})^2}{2}))} \tag{4.6}$$

The two signals from two cars are summed up as one general received signal $s_r(t)$ at the victim radar receiver. The total received signal in the victim radar is defined as

$$s_r(t) = s_{tr}(t) + s_{rint}(t). \tag{4.7}$$

4.1.2. DECHIRPING

The target reflection signal is attenuated too much by bidirectional propagation in the free space, dechirping helps maintain the acceptable signal-to-interference ratio (SIR). By applying the dechirping, the receiver signal $s_r(t)$ is multiplied with the conjugate of the transmitted signal through the mixer [17]. The signal after the mixer $s_m(t)$ can be computed as

$$\begin{aligned} s_m(t) &= s_r(t) e^{2j\pi(f_c t + \frac{k}{2}t^2)} \\ &= (\sqrt{P_{int}} e^{-2j\pi(f_{intc}t + \frac{k_{int}(t-\tau_{int})^2}{2})} + \sqrt{P_{tr}} e^{-2j\pi(f_c(t-\tau) + \frac{k(t-\tau)^2}{2})}) e^{2j\pi(f_c t + \frac{kt^2}{2})} \\ &= \sqrt{P_{tr}}(e^{\pi j(2k\tau t - k\tau^2 + 2f_c\tau)}) + \sqrt{P_{ir}} e^{\pi j((k-k_{int})t^2 - k_{int}\tau_{int}^2 + 2f_{intc}\tau_{int} + 2(k_{int}\tau_{int} + f_c - f_{intc})t)} \end{aligned} \tag{4.8}$$

The first term of the equation is the same as Equation 2.6, which represents the target component. The beat frequency of the target component depends on $k\tau$. As for the second term, the frequency of the interference component is influenced by the difference between the slopes $k_{int} - k$ and $k_{int}\tau_{int} + f_c - f_{intc}$.

4.1.3. FAST-TIME FOURIER TRANSFORM DERIVATION

For range estimation, the Fourier transform in fast time is applied to the output signal after dechirping. $S_m(f)$ denotes the mixer output signal in the frequency domain. It can be obtained by

$$
\begin{aligned}
S_m(f) &= \int_0^T s_m(t) e^{-2j\pi f t} dt \\
&= \sqrt{P_{tr}} \int_0^T e^{j\pi(2k\tau t - k\tau^2 + 2f_c\tau)} e^{-2j\pi f t} dt \\
&+ \sqrt{P_{ir}} \int_0^T e^{j\pi((k-k_{int})t^2 + 2(f_c - f_{intc} + k_{int}\tau_{int})t - k_{int}\tau_{int}^2 + 2f_{intc}\tau_{int})} e^{-2j\pi f t} dt.
\end{aligned} \tag{4.9}
$$

The first term of (4.9) is the target component and can be calculated as follows:

$$
\begin{aligned}
S_{target}(f) &= \sqrt{P_{tr}} \int_0^T e^{j\pi(2k\tau t - k\tau^2 + 2f_c\tau)} e^{-2j\pi f t} dt \\
&= \sqrt{P_{tr}} \int_0^T e^{2j\pi((k\tau - f)t - \frac{1}{2}k\tau^2 + f_c\tau)} dt \\
&= \sqrt{P_{tr}} e^{j\pi(2f_c\tau - k\tau^2)} \frac{1}{2j\pi(k\tau - f)} (e^{(2j\pi(k\tau - f)T} - 1)
\end{aligned} \tag{4.10}
$$

The second term of (4.9) is the interference component. It can be solved by

$$
\begin{aligned}
S_{int}(f) &= \sqrt{P_{ir}} \int_0^T e^{j\pi((k-k_{int})t^2 + 2(f_c - f_{intc} + k_{int}\tau_{int})t - k_{int}\tau_{int}^2 + 2f_{intc}\tau_{int})} \cdot e^{-2j\pi f t} dt \\
&= \sqrt{P_{ir}} e^{j\pi(2f_{intc}\tau_{int} - k_{int}\tau_2^2)} \int_0^T e^{j\pi(k-k_{int})t^2 + 2j\pi(k_{int}\tau_{int} + f_c - f_{intc} - f)t} dt \\
&= \sqrt{P_{ir}} e^{j\pi(2f_{intc}\tau_{int} - k_{int}\tau_{int}^2)} \int_0^T e^{-(j\pi(k_{int}-k))t^2 - 2j\pi(k_{int}\tau_{int} + f_c - f_{intc} - f)t)} dt
\end{aligned} \tag{4.11}
$$

Substituting $\sqrt{j\pi(k_{int} - k)} = \alpha$ and $j\pi(k_{int}\tau_{int} + f_c - f_{intc} - f) = f_b$ into 4.11, 4.11 turns out

$$
\begin{aligned}
S_{int}(f_b) &= \sqrt{P_{ir}} e^{j\pi(2f_{intc}\tau_{int} - k_{int}\tau_{int}^2)} \int_0^T e^{-(\alpha^2 t^2 - 2f_b t)} dt \\
&= \sqrt{P_{ir}} e^{j\pi(2f_{intc}\tau_{int} - k_{int}\tau_{int}^2)} \int_0^T e^{-(\alpha^2 t^2 - 2f_b t + (\frac{f_b}{\alpha})^2 - (\frac{f_b}{\alpha})^2)} dt \\
&= \sqrt{P_{ir}} e^{j\pi(2f_{intc}\tau_{int} - k_{int}\tau_{int}^2)} \int_0^T e^{-(\alpha t - \frac{f_b}{\alpha})^2 + (\frac{f_b}{\alpha})^2} dt \\
&= \sqrt{P_{ir}} e^{j\pi(2f_{intc}\tau_{int} - k_{int}\tau_{int}^2)} e^{(\frac{f_b}{\alpha})^2} \int_0^T e^{-(\alpha t - \frac{f_b}{\alpha})^2} dt
\end{aligned} \tag{4.12}
$$

Take $x = \alpha t - \frac{f_b}{\alpha}$ and $dx = \alpha dt$, 4.12 can be written as

$$
S_{int}(f_b) = \sqrt{P_{ir}} e^{j\pi(2f_{intc}\tau_{int} - k_{int}\tau_{int}^2)} e^{(\frac{f_b}{\alpha})^2} \int_{-\frac{f_b}{\alpha}}^{\alpha T - \frac{f_b}{\alpha}} e^{-(x)^2} dx/\alpha \tag{4.13}
$$

According to the Gauss error function, the integral of 4.13 is

$$S_{int}(f_b) = \frac{\sqrt{P_{ir}}}{\alpha} e^{j\pi(2f_{intc}\tau_{int} - k_{int}\tau_{int}^2)} e^{(\frac{f_b}{\alpha})^2} (\frac{1}{2}\sqrt{\pi}(erf(\alpha T - \frac{f_b}{\alpha}) - erf(-\frac{f_b}{\alpha}))) \tag{4.14}$$

where erf is the error function defined by:

$$erf(z) = \frac{2}{\sqrt{\pi}} \int_0^z e^{(-t^2)} dt \tag{4.15}$$

Thus,

$$\begin{aligned} S_m(f) &= S_{target}(f) + S_{int}(f) \\ &= \frac{\sqrt{P_{tr}} e^{j\pi(2f_c\tau - k\tau^2)}}{2j\pi(k\tau - f)} (e^{(2j\pi(k\tau - f)T)} - 1) + \\ &\frac{\sqrt{P_{ir}} e^{j\pi(2f_{intc}\tau_{int} - k_{int}\tau_{int}^2)}}{\sqrt{j\pi(k_{int} - k)}} e^{(\frac{j\pi(k_{int}\tau_{int} + f_c - f_{intc} - f)}{\sqrt{j\pi(k_{int} - k)}})^2} (\frac{1}{2}\sqrt{\pi}(erf(\sqrt{j\pi(k_{int} - k)}T - \\ &\frac{j\pi(k_{int}\tau_{int} + f_c - f_{intc} - f)}{\sqrt{j\pi(k_{int} - k)}}) - erf(-\frac{j\pi(k_{int}\tau_{int} + f_c - f_{intc} - f)}{\sqrt{j\pi(k_{int} - k)}}))) \end{aligned} \tag{4.16}$$

4.1.4. SLOW-TIME FOURIER TRANSFORM DERIVATION

To obtain the range-Doppler profile, multiple chirps are investigated. Assume that N chirps from the victim radar are sent in one CPI and the relative velocity of the target car and the interfering car is v_{target} and v_{int}. Due to the velocity difference, the Doppler effect is introduced by adding the item $e^{2j\pi\frac{2v_{target}}{\lambda}nT}$ [38]. Moreover, multiple chirps are sent; thus, the time expression is also changed to $t = nT + t'$, in which n is the number of the chirp, T is the chirp duration and t' is the interfering time. Substitute t into this expression with respect to n. The signal after mixer turns to :

$$\begin{aligned} s_m(n, t') = &\sqrt{P_{tr}} e^{j\pi(2k\tau t' - k\tau^2 + 2f_c\tau)} e^{2j\pi\frac{2v_{target}}{\lambda}nT} + \\ &\sqrt{P_{ir}} e^{j\pi((k - k_{int})t'^2 + 2(f_c - f_{intc} + k_{int}\tau_{int})t' - k_{int}\tau_{int}^2 + 2f_{intc}\tau_{int})} e^{2j\pi\frac{v_{int}}{\lambda}nT} \end{aligned} \tag{4.17}$$

Along with a similar method from the last section, the signal after fast time Fourier transform is :

$$\begin{aligned} S_m(n, f) = &\frac{\sqrt{P_{tr}} e^{j\pi(2f_c\tau - k\tau^2)}}{2j\pi(k\tau - f)} (e^{(2j\pi(k\tau - f)T} - 1) e^{2j\pi\frac{2v_{target}}{\lambda}nT} + \\ &\frac{\sqrt{P_{ir}}}{\alpha} e^{j\pi(2f_{intc}\tau_{int} - k_{int}\tau_{int}^2)} e^{(\frac{f_b}{\alpha})^2} (\frac{1}{2}\sqrt{\pi}(erf(\alpha T - \frac{f_b}{\alpha}) \\ &- erf(-\frac{f_b}{\alpha}))) e^{2j\pi\frac{v_{int}}{\lambda}nT} \end{aligned} \tag{4.18}$$

When reaching the Doppler profile, the Fourier transform is applied to the slow time with respect to the numbers of the chirps, n.

If the chirp duration of the interference signal is the same as that of the victim radar, then, the range-Doppler map for such an interference case can be derived as follows:

$$\begin{aligned}
S_{2d}(f,f_d) &= \frac{\sqrt{P_{tr}}e^{j\pi(2f_c\tau-k\tau^2)}}{2j\pi(k\tau-f)}(e^{(2j\pi(k\tau-f)T}-1)\int_0^{N-1} e^{2j\pi\frac{2v_{target}}{\lambda}nT}e^{-2j\pi f_d n}dn+\\
&\frac{\sqrt{P_{ir}}}{\alpha}e^{j\pi(2f_{intc}\tau_{int}-k_{int}\tau_{int}^2)}e^{(\frac{f_b}{\alpha})^2}(\frac{1}{2}\sqrt{\pi}(erf(\alpha T-\frac{f_b}{\alpha})\\
&-erf(-\frac{f_b}{\alpha})))\int_0^{N-1} e^{2j\pi\frac{v_{int}}{\lambda}nT}e^{-2j\pi f_d n}dn\\
&=\frac{\sqrt{P_{tr}}e^{j\pi(2f_c\tau-k\tau^2)}}{2j\pi(k\tau-f)2j\pi(\frac{2v_{target}T}{\lambda}-f_d)}(e^{(2j\pi(k\tau-f)T}-1)(e^{2j\pi(\frac{2v_{target}T}{\lambda}-f_d)(N-1)}-1)+\\
&\frac{\sqrt{P_{ir}}}{\alpha(2j\pi(\frac{v_{int}T}{\lambda}-f_d))}e^{j\pi(2f_{intc}\tau_{int}-k_{int}\tau_{int}^2)}e^{(\frac{f_b}{\alpha})^2}(\frac{1}{2}\sqrt{\pi}(erf(\alpha T-\frac{f_b}{\alpha})\\
&-erf(-\frac{f_b}{\alpha})))(e^{2j\pi(\frac{v_{int}T}{\lambda}-f_d)(N-1)}-1)
\end{aligned} \tag{4.19}$$

If the chirp duration of the interference signal is integer times for the victim radar, the Fourier transform on one chirp can be considered as m=$\frac{T}{T_{int}}$ sectors for the calculation of the interference component. This type of interference is called periodically asynchronous interference and its range-Doppler map can be found as:

$$\begin{aligned}
S_{2dint}(f,f_d,m) &= \sum_{q=0}^{m-1}\frac{\sqrt{P_{ir}}}{\alpha}e^{j\pi(2f_{intc}\tau_{int}-k_{int}\tau_{int}^2)}e^{(\frac{f_b}{\alpha})^2}(\frac{1}{2}\sqrt{\pi}(erf((q+1)\alpha T_{int}-\frac{f_b}{\alpha})\\
&-erf(q\alpha T_{int}-\frac{f_b}{\alpha})))\int_0^{N-1} e^{2j\pi\frac{v_{int}}{\lambda}nT}e^{-2j\pi f_d n}dn\\
&=\sum_{q=0}^{m-1}\frac{\sqrt{P_{ir}}}{\alpha(2j\pi(\frac{v_{int}T}{\lambda}-f_d))}e^{j\pi(2f_{intc}\tau_{int}-k_{int}\tau_{int}^2)}e^{(\frac{f_b}{\alpha})^2}\\
&(\frac{1}{2}\sqrt{\pi}(erf((q+1)\alpha T_{int}-\frac{f_b}{\alpha})-erf(q\alpha T_{int}-\frac{f_b}{\alpha})))(e^{2j\pi(\frac{v_{int}T}{\lambda}-f_d)N-1}-1)
\end{aligned} \tag{4.20}$$

where $f_b = j\pi(\frac{qB}{m}+k_{int}\tau_{int}+f_c-f_{intc}-f)$. Here, f_b is changing according to the number of sectors in one chirp m and the sequence of the chirps q.

4.2. EXAMINATION OF THE MATH MODEL

In this section, the mathematical models from Section 4.1 are examined and compared with the analytical model simulation based on the MATLAB functions. Considering the bandwidths and chirp duration of the victim radar signal and the interference radar signal, all interference situations can be classified by *synchronous* and *asynchronous*. Synchronous interference means the interference signal has the same chirp duration as the victim signal. Asynchronous interference means the interference signal has a different chirp duration than the victim signal.

Furthermore, in synchronous cases, there is a special case called the fully synchronous case, which means that the two signals not only have the same chirp time duration but also have the same bandwidth. As for the asynchronous situation, it can be divided into 2 types, periodic and aperiodic. In the periodical situation, the victim signal's chirp duration is multiple of the interference signal, and in this situation the mathematical equation is achievable. For the aperiodic situation, the pattern of time looks quite random, thus, only the numerical simulation result of this case is investigated in this thesis. The classification of all cases is listed in Table 4.1.

Interference Cases	**Condition for T and B**
Fully synchronous	Same T and B
General synchronous	Same T, different B
Periodic asynchronous	T_{target} multiple to T_{int}, different B
Aperiodic asynchronous	Different T (not multiple), different B

Table 4.1: Different cases with respect to bandwidth and chirp duration

All the cases mentioned above (except for the aperiodic asynchronous case) are processed by numerical simulation on the analytical model and MATLAB analytical model simulation with the same input to verify the mathematical models and investigate the interference behavior in different cases.

Parameter	**Value**
$f_c = f_{intc}$	77 GHz
f_s	1 GHz
G_t	30 dB
G_r	20 dB
P_t	30 dB
B	300 MHz
T	25.6μs
G_{tint}	10 dB
P_{tint}	10 dB
N_p	108

Table 4.2: FMCW signal model parameters

The common radar parameters used for all cases are listed in Table 4.2. The victim radar parameters are the same as the simulation given in interference-free cases in Chapter 3. In addition, f_{intc} is the center frequency of the interference radar. In these simulations, it is set to the same value as the victim radar. G_{tint} and P_{tint} denote the antenna gain and the transmission power of the interference radar. The number of chirps that are sent in CPI in the simulations, N_P=108.

4.2.1. FULLY SYNCHRONOUS

In the fully synchronous cases, interference and victim FMCW radar signals are assigned the same bandwidth $B = B_{int} = 300$ MHz and chirp time $T = T_{int} = 25.6\ \mu s$. Assume that the target car is R=100 m from the interference radar and R_{int}=300 m from the victim radar. The relative velocity of the target car, V_{target}=10 m/s and for the interference car, V_{int} =20 m/s. After transmission, the reflection signal and the interference signal are received at the receiver.

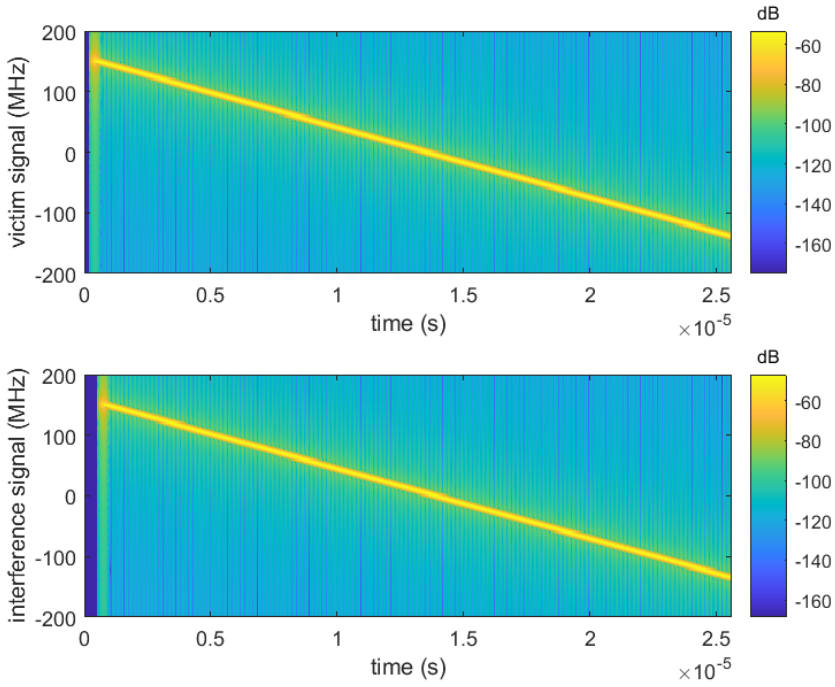

Figure 4.2: Spectrum of the received signals in the fully synchronous case

Due to the difference in the distance, as shown in Figure 4.2, the spectrum of two signals start at different time. The time delay of the victim signal and interference signal at the receiver is τ=0.667 μs and τ_{int}=1 μs, respectively. In this case, they all start at half of the bandwidth. The frequency increases linearly over time with the same slope.
Figures 4.3 show the results of the Fourier transform in fast time generated by applying the numerical simulation and equations simulation, respectively. In both figures, two spikes are located at 100 and 150 m. 100 m is the range of the target, and 150 m is half of the interference's range, which is calculated only one-way. The amplitude level of the target spike is around -101 dB which matches the theoretical value A_{tr}=-101.6 dB obtained by

$$A_{tr} = \sqrt{P_t P_{tr}} \tag{4.21}$$

where P_{tr} is computed from Equation 4.2. For the interference spike, the theoretical

value of the amplitude level A_{tr}=-95.12 dB is calculated from Equation 4.5. The two spikes are also reflected in the range-Doppler map, as shown in Figure 4.4. The cells that contain the highest power are the cells in the range of 100 m and 150 m with a velocity equal to 10 m/s. For the same reason as in the calculation of the interference range, the value of the velocity of the interference on the Doppler range map is also halved.

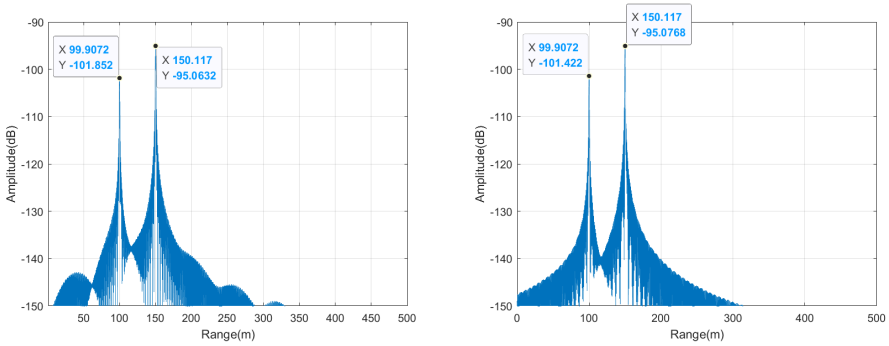

(a) Fast time result from the numerical simulation

(b) Fast time result from the analytical model simulation

Figure 4.3: Fully synchronous case fast time results generated by numerical simulation(a) and analytical model simulation(b)

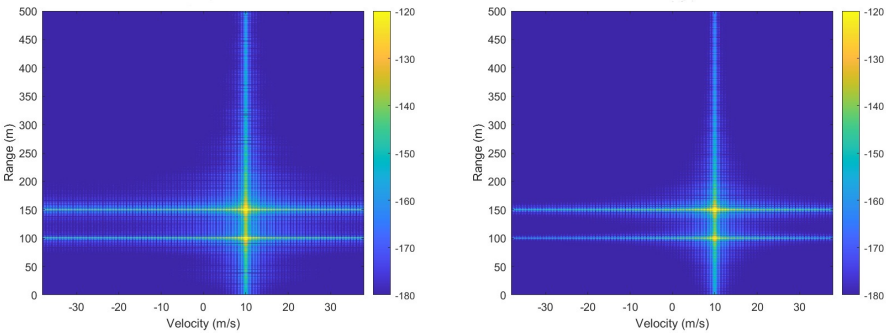

(a) Range-Doppler result from the numerical simulation

(b) Range-Doppler result from the analytical model simulation

Figure 4.4: Fully synchronous case Range-Doppler results generated by numerical simulation(a) and analytical model(b)

In this case, the interference signal can be considered as another target, a situation similar to the cases of multiple targets explained in Section 3.5. Although this kind of interference signal, called ghost target, is difficult to occur, it may cause miss detection and false alarm and lead to driving safety problems.

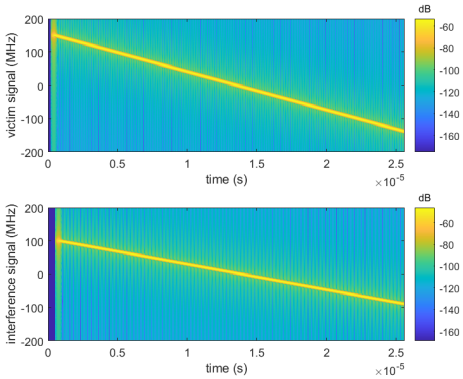

Figure 4.5: Spectrum of the received signals in the general synchronous case

4.2.2. GENERAL SYNCHRONOUS

The fully synchronous cases are the special cases because not all automotive radars have the same bandwidth, chirp duration and chirp slopes. To realize the general synchronous case, the bandwidth of the interference radar changes to B_{int}=200 MHz to make the difference; Meanwhile, the chirp duration of the victim radar and the interference radar remain unchanged $T = T_{int} = 25.6\ \mu s$. Distance and relative velocities keep the same values as in fully synchronous situations. Since the B= 300 MHz, the slope of victim signal k= 11.7188 is higher than the interference signal k_{int}= 7.8125. As shown in Figure 4.5, the victim signal has a steeper slope than the interference signal. The distance hasn't changed, therefore, the time delay of two signals remains the same as in the fully synchronous case.

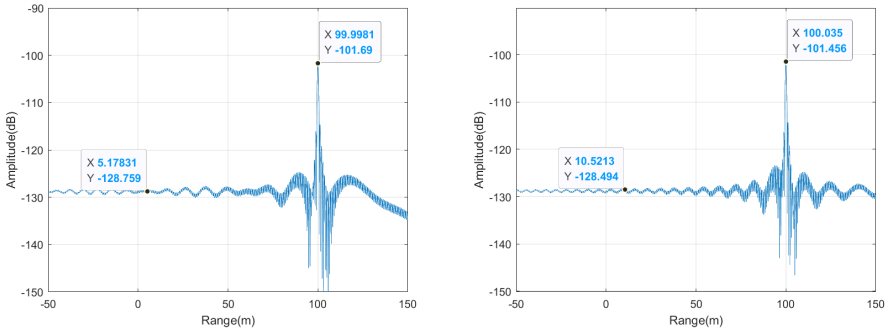

(a) Fast time result from the numerical simulation

(b) Fast time result from the analytical model simulation

Figure 4.6: General synchronous case fast time results generated by numerical simulation(a) and analytical model simulation(b)

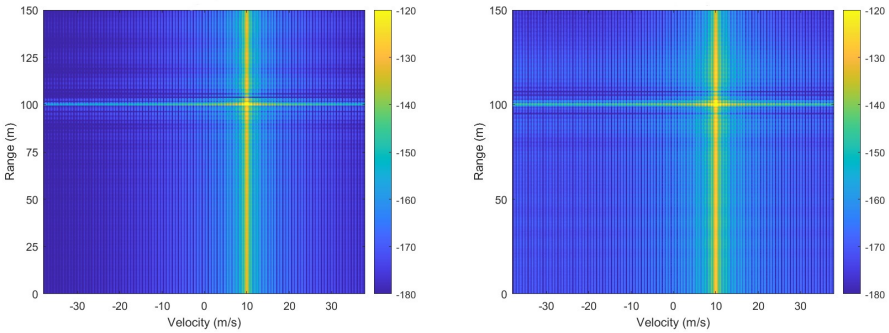

(a) Range-Doppler result from the numerical simulation

(b) Range-Doppler result from the analytical model simulation

Figure 4.7: General synchronous case Range-Doppler results generated by numerical simulation(a) and analytical model simulation(b)

In Figures 4.6, they are shown that instead of the ghost target, the interference spreads over the frequency domain, which looks like the noise floor. The noise-like interference amplitude level is around -128.5 dB according to Figure 4.6. The target spike is still at the desired place with an amplitude level of approximately -101 dB. Thus, in the range profile, only the target spike is left, and it is located in the range of 100 m.

If a 20MHz low-pass filter is applied, the interference signal may not be fully captured. The amount of the interference signal that is captured varies depending on the bandwidth of the interference signal. When the interference signal's bandwidth is closer to the victim signal's bandwidth, a longer portion of the interference signal is captured. For example, when the interference signal's bandwidth is 100MHz, 150MHz, 200MHz, and 300MHz, 5.37μs, 7.2/microseconds, 10.56μs, and 25.2μs of the interference signal is captured in one chirp as it shown in the Figure 4.8, respectively. Compared to the chirp duration of the victim signal, this corresponds to 20.98%, 28.13%, 41.6%, and 98.43%, respectively.

The level of processed interference varies depending on the amount that is captured, as depicted in the Figure 4.10. When the bandwidth of the interference signal is 100MHz, 150MHz, 200MHz, and 300MHz, the amplitude levels are -227.097, -226.025, -224.512, and -192.1dB, respectively. When a larger portion of the interference signal is captured, the interference level is higher. As it shown in Figure 4.9 observed that the amplitude of interference is almost linearly increased based on the percentage of signal captured, except for the fully synchronous case.

During the first FFT processing, both the signal and interference components are impacted by processing gains G_s and G_i, as shown in Equation 4.22.

$$G_s = BT \equiv 38.85dB, G_i = 1 \equiv 0dB \tag{4.22}$$

The signal processing gain G_s for the target response is determined by BT and equals to

38.85dB. In case of narrowband interference, the difference between the target response in its maximum and the interference level is approximately 40dB. As the bandwidth of the interference signal increases, the level of interference in the beat frequency signal also increases in a linear manner. This leads to a longer duration of the interference's presence in the spectrogram of the beat frequency signal. This continues until the interference becomes almost perfectly synchronized with the victim radar which resulting in the appearance of a ghost target. However, at the moment of fully synchronous, the level of interference jumps to -192 dB and the linearity doesn't exist. Thus, except for the fully synchronous case, the qualitative description of this process can be represented by the overlap factor of the signal and interference at the beat frequency, denoted as

$$O = T_{intcaptured} / T. \tag{4.23}$$

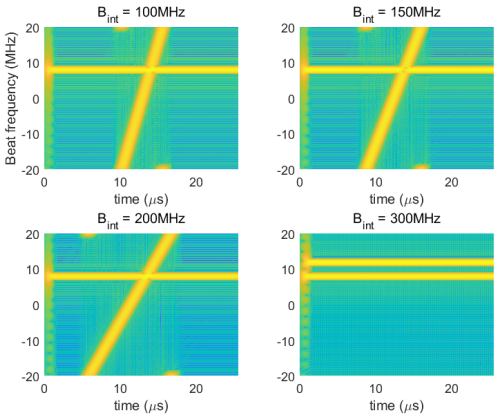

Figure 4.8: Beat frequency with respect to different B_{int} in general synchronous cases

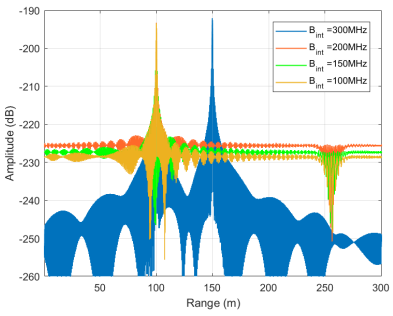

Figure 4.9: The amplitude level of processed interference with respect to different interference bandwidth

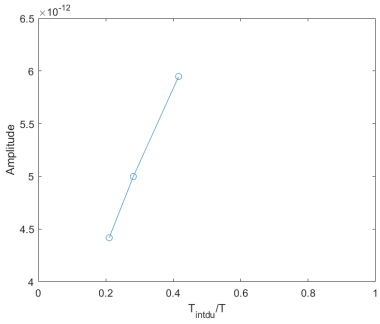

Figure 4.10: The amplitude level of processed interference with respect to portion that captured

The output of signal processing varies based on the bandwidth of the interference signal. As shown in Figure 4.11, the bandwidth of the victim signal is 300 MHz. When the value of B_{int} is getting closer to the victim signal, SIR decreased symmetrically. Especially, when B_{int}=B=300 MHz (fully synchronous case), SIR reaches the lowest value. This is because the interference power is centralized as a target in the fully synchronous case.

Besides, in the range-Doppler domain, which is shown in Figure 4.7, the cells containing the highest power are in the range of around 100 m and with a velocity of 10 m/s. The interference component in the velocity profile is concentrated at 10 m/s. For the interference signal, the value of the velocity profile is doubled, which is 20 m/s in the example. Comparison of the simulation results of 2D-FFT from two methods (numerical and equation-based) validated the derived analytical model for the general synchronous cases.

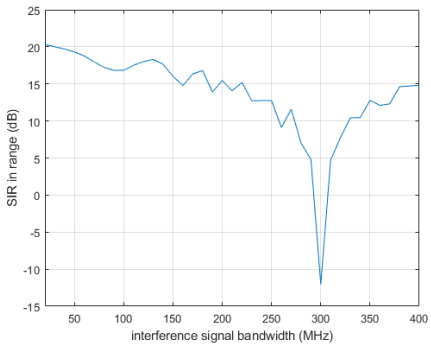

Figure 4.11: SIR with respect to different B_{int} in general synchronous cases with Np=108

4.2.3. PERIODICAL ASYNCHRONOUS

In real life, the chirp duration of FMCW radars can also be different. If the chirp duration of the interference radars is an integer multiple of the victim radar, the analytical expression can also be applied to obtain the information on the range and velocity as given in 4.20.
In this verification, the chirp duration of the interference radar signal is given by half of the victim radar signal, $T_{int}=\frac{T}{2}=\frac{25.6\mu s}{2}$=12.8 μs. The bandwidth remains the same as for general synchronous cases, B = 300 MHz and B_{int} = 200 MHz. The relative range and velocity of the target and interference car are kept the same as in the general synchronous case simulations.

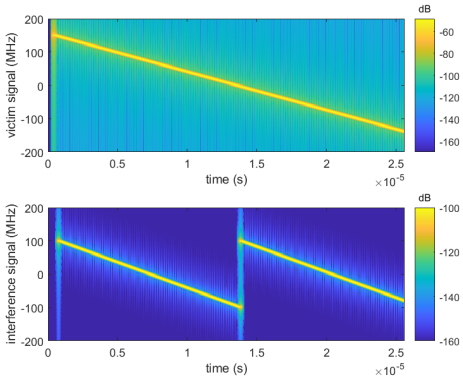

Figure 4.12: Spectrum in the periodic asynchronous case

As shown in Figure 4.12, the transmitted signal's frequency decreases 300 MHz in one chirp duration T. As for the interference signal, after the frequency drop B_{int}=200 MHz, it starts the second chirp immediately. Since the chirp duration of the interference signal is half the transmitted signal, the second chirp starts from t=$\frac{T}{2}$=12.8 μs and there are a total of two full chirps of the interference signal in one transmitted signal chirp duration. It is illustrated in Figure 4.13, the target component formulated a spike at 100 m in the range profile with an amplitude level of around -101 dB, which is similar to the synchronous case. The interference component is also spread like noise. In the range-Doppler map, as shown in Figure 4.14, both the target and interference power are laid at 10 m/s(half of the true velocity of the interference). In addition, the results of the fast time FFT and the range-Doppler from equations are consistent with the analytical model simulation method and they support the validation of Equation 4.20.

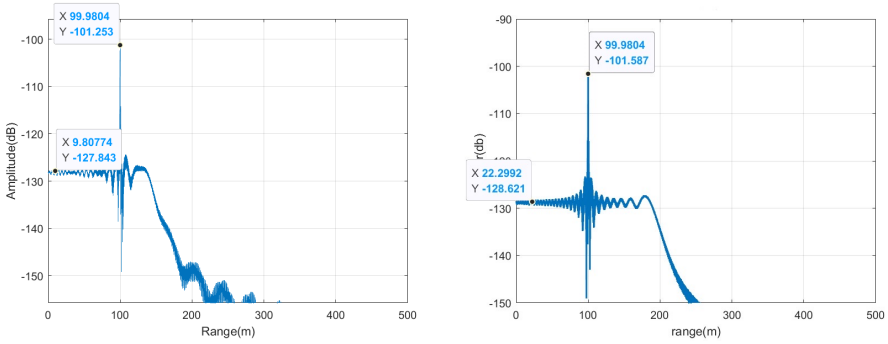

(a) Fast time result from the numerical simulation

(b) Fast time result from the analytical model simulation

Figure 4.13: Periodical asynchronous synchronous case fast time results generated by numerical simulation(a) and analytical model simulation(b)

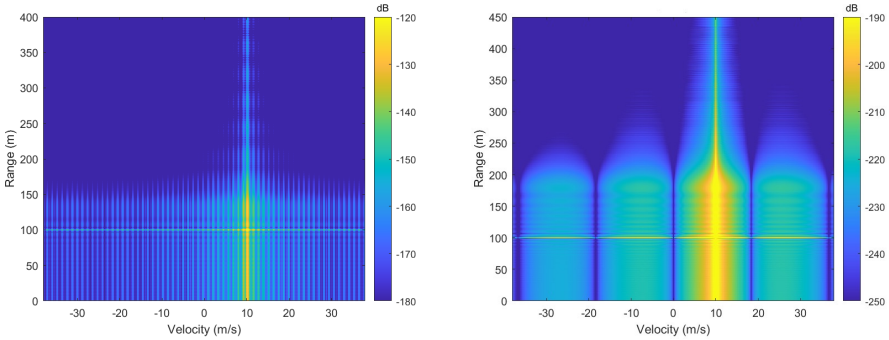

(a) Range-Doppler result from the numerical simulation

(b) Range-Doppler result from the analytical model simulation

Figure 4.14: Periodical asynchronous case Range-Doppler results generated by numerical simulation(a) and analytical model simulation(b)

4.2.4. APERIODIC ASYNCHRONOUS

In aperiodic asynchronous cases, the chirp time of the victim and the interference radar signal are primes of each other. In this verification, the chirp duration of the interference radar signal is $T_{int} = 10.8\ \mu$ s and the transmitted and interference signal bandwidths are $B = 300$ MHz and $B_{int} = 200$ MHz. All other parameters are kept the same as in Section 4.2.3. In this case, the numerical math model is not derived in this thesis. Thus, the following results are from numerical simulation only.

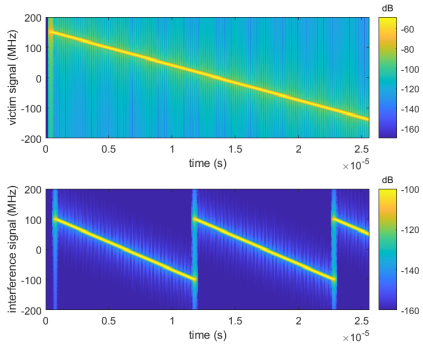

Figure 4.15: Spectrum for interfering radar and victim radar signal in the aperiodic asynchronous case

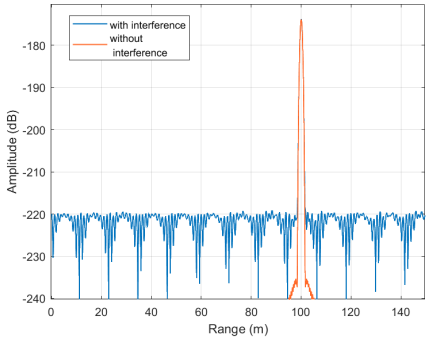

Figure 4.16: Range profile obtained via numerical simulations of the aperiodical asynchronous interference with power 10 dB

As shown in Figure 4.15, the interference signal ends around 60 MHz in the first transmitted signal chirp. In the next chirp of the victim signal, the interference signal continues the chirp procedure from the end place of the last transmitted signal chirp, and the frequency will continuously decrease from 60 MHz to -100 MHz.

After propagation, the received signal has a power of P_{tr} = -101.63 dB, while the interference power is P_{ir} = -99.72 dB. The SIR before any processing is sir = P_{tr} - P_{ir} = 1.9 dB. During the first FFT processing, both the signal and interference components are impacted by processing gains $G_s = BT \equiv 38.85dB$ and $G_i = 1 \equiv 0dB$.

As for slow time, a Chebyshev window at the length of 80 points is applied to reduce the sidelobes. After 2D-FFT, the interference is spread over not only in the range domain but also the Doppler domain. Thus, a Doppler processing loss L_D is applied to the interference component as it shown in Equation 4.24

$$L_D = N_p = 108 \equiv 20.33dB \tag{4.24}$$

Overall, SIR after 2D-FFT with the aperiodical asynchronous interference

$$SIR = sir + G_s + L_D = 61.08dB \tag{4.25}$$

Figure 4.16 shows the target and interference components in the range profile with a cut of 2D-FFT result on the 10m/s velocity profile. It is observed that the interference is transferred to noise floor like multiple low-power spikes after 2D-FFT processing. This is the consequence of two FMCW radar signals being totally unrelated in chirp duration, and the beat frequencies of all interference chirps will have arbitrary values in the range domain. Similarly in the Doppler domain, from Figure 4.17, it can be noted that the interference is not a ridge over a velocity profile of 10 m/s as in all other cases, but turns into multiple random cells in both the range and the Doppler domain. Nevertheless, the target component remains constant as a spike in the 100 m range with a velocity of 10 m/s, which is the same as in other cases.

The processed interference has an average level of A_{int} = -219.22 dB, while the peak level of the target component is A_{target} = -173.83 dB. As a result, the signal-to-interference

ratio (SIR) can be calculated as SIR = A_{target} -A_{int} = 47.06 dB, which has 14 dB difference with the analysis. There are two main reasons for the observed differences between the analytical analysis and simulation results in this case. The first reason is related to the amount of interference signal that is captured. As it explained in the general synchronous case, due to the low-pass filter, not all of the interference signal is captured, resulting in a loss of interference power.The SIR overlap factor O at the beat frequency plays a role. In the aperiodic asynchronous case, it is difficult to provide an analysis model for the distribution of the captured interference signal, and thus it is not included in this thesis. The second reason is that the captured interference signal is not fully staggered from chirp to chirp. This means that Doppler processing will be part coherent, leading to overlaps. L_D should have a lower value compared to N_p. Both of these reasons contribute to the differences between the analytical analysis and simulation results in this study.

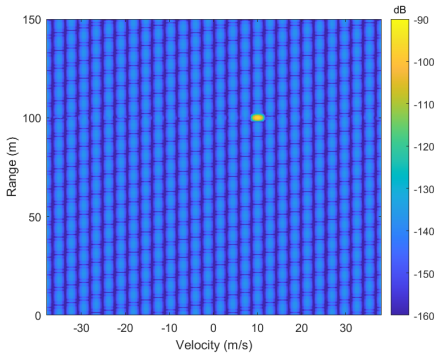

Figure 4.17: Range-Doppler representation of the received signal obtained via numerical simulations of the aperiodical asynchronous interference with power 10 dB

4.3. CONCLUSION

In the first section 4.1, the signal model of FMCW-to-FMCW mutual interference is built. The mathematical expressions on the signal after dechirping, Fourier transform in fast time and slow time are derived. For Doppler processing, i.e. the slow time Fourier transform, the interference behavior is classified as synonymous and asynchronous. In the second section 4.2, the equations from the first section are validated by comparing the numerical simulation with the analytical model simulation. To better understand the interference behavior, the results are presented in four cases: fully synchronous, general synchronous, periodic asynchronous, and aperiodic asynchronous.

The behaviour of the investigated interference cases in 2D range-Doppler as follows. In the fully synchronous case, the received interference energy concentrates at one particular range-Doppler cell, resulting in a ghost target which can not be distinguished from the real target. In both the synchronous and periodic asynchronous cases, interference results in the presence of a noise-like ridge which is distributed across the range profile. The corresponding velocity profile, on the other hand, shows a centralized dis-

tribution of the noise-like ridge. The amplitude of the processed signal is primarily influenced by the signal processing gain, which is determined by the product of the bandwidth and chirp duration BT for the target response and the SIR overlap factor O at the beat frequency for interference component. Additionally, as the bandwidth of the interference increases, the interference level in the beat frequency signal also increases linearly with its bandwidth. This results in a longer presence of the interference in the spectrogram of the beat frequency signal.

In the aperiodic asynchronous case, the interference power is randomly spread over the range-Doppler map due to the incoherent chirp duration. Overall, except for the fully synchronous case, the power of the target component is prominent in the frequency domain and the interference power will be degraded during the FMCW processing procedure. The SIR of processed signal in the aperiodic asynchronous case is determined by several factors. These include: a) the ratio between the power of the target response and interference at the input of the receiver. b) O at the beat frequency after the mixer and low-pass filter. c) signal processing gain G_s for the target response. d) signal processing gain for the coherent Doppler processing.

5

PERFORMANCE ANALYSIS

In this chapter, the performance of CFAR detection on FMCW-to-FMCW mutual interference is analyzed. The CFAR detection algorithm that was performed in this thesis is introduced in Section 5.1. The CFAR detection results of different interference cases and the corresponding analysis of the relationship between the probability of detection P_d, probability of false alarmP_{FA} and SIR are presented in Section 5.2 by Receiver Operating Characteristic (ROC) curves.

5.1. CFAR DETECTION ALGORITHM

CFAR has become one of the most widely used detection methods in the radar system. The working principle of this algorithm is to determine the power threshold by giving the constant false alarm rate [2]. If the threshold is extremely high, even above the power of the target spike, a miss-detection problem will be raised. On the other hand, if the threshold is too low, then interference or noise will likewise be detected as targets, causing the problem of false alarms.

The input of the CFAR algorithm is the range-Doppler map in this thesis. In total, there are 10240×64 cells corresponding to the number of samples in the range and the Doppler profile, respectively. The input cells on the range-Doppler map will be tested by several 2D CFAR windows as shown in Figure 5.1. Here, x_i is the test cell, which has higher power than the threshold and will be detected as 1 [39]. In contrast, if x_i has a power lower than the threshold, it will be considered 0. The threshold T_{cfar} is determined by 2 parameters as shown in Equation 5.1, the mean power in the CFAR window P_n and a scaling factor α [40] [41].

$$T_{cfar} = \alpha P_n \tag{5.1}$$

The value of the scaling factor depends on the desired false alarm rate P_{FA} and the number of cells in one CFAR window, as shown in Equation 5.2 [42]. When the 2D CFAR window is determined, the threshold is only affected by the desired P_{FA}. Higher P_{FA} is

given, the lower threshold will be applied to the detector.

$$\alpha = N_{window}(P_{FA}^{\frac{-1}{N_{window}}} - 1) \tag{5.2}$$

One 2D CFAR window consists of 3 parts, the test cell itself, the guard cells and the reference cells. Guard cells surround the test cell to ensure that the test is not influenced by nearby cells similar to the test cell, and they are not taken into account to calculate the threshold [43]. In this thesis, the guard band size in the range profile is 3 cells and 5 cells in the Doppler profile.

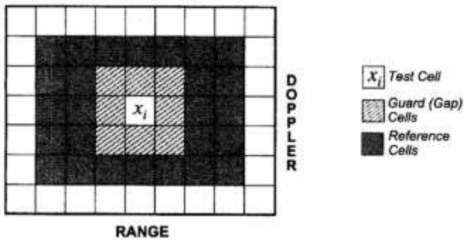

Figure 5.1: 2D CFAR window [2]

Outside the guard band are the reference cells. They are the training cells to obtain the corresponding threshold. 5 and 10 cells are taken as reference in the range and Doppler domain, respectively. Due to the existence of the guard band and the reference cells, the cells located at the edges of the map are not possible to be tested. On the range axes, counting from both edges, 16 cells (double the sum of 3 guard cells and 5 reference cells) should not be included as the test cells. Similarly, on the Doppler axes, 30 cells are not included.

In addition to the CFAR window, another important factor in this algorithm is the reference. The decision is made referring to the existence of the target in this thesis. The null hypothesis (H0) and the alternative hypothesis (H1) are the combinations of signals associated with noise, interference and target echo as follows:

- **H0** : noise + interference
- **H1** : noise + interference + target

5.2. DETECTION RESULTS IN DIFFERENT CASES

Referring to Chapter 4, CFAR detection is performed for three interference scenarios: fully synchronous, general synchronous and asynchronous. Fully synchronous and general synchronous cases have the same definition as mentioned in Chapter 3. Here, the asynchronous case refers to the fully asynchronous case. For all three cases, the range and velocity values for the target and interference remained constant, R_{target}=50 m, R_{target}=20 m/s, R_{target}=250 m, and V_{int}=40 m/s. The relative amplitude level of noise at the input is 35 dB. The other target and interference signal parameters for three cases

are listed in Table 5.1. The input range-Doppler plane is generated by 64 processed chirps. The amplitude level of the target at the receiver, before processed, assumed as 0 dB amplitude level is given from referring to Chapter 4. CFAR detection is performed for three interference scenarios: fully synchronous, general synchronous and asynchronous. Fully synchronous and general synchronous cases have the same definition as mentioned in Chapter 3. Here, the asynchronous case is the fully asynchronous case. For all three cases, the range and velocity values for the target and interference remained constant, R_{target}=50 m, R_{target}=20 m/s, R_{target}=250 m, and V_{int}=40 m/s. The other target and interference signal parameters for three cases are listed in Table 5.1. The input range-Doppler plane is generated by 64 processed chirps. The amplitude level of the target and at the receiver, before processing is 0 dB. As for the interference, the amplitude levels at the receiver is changed between the interval from 20 dB to 55 dB.

	Cases	**Range (m)**	**Velocity (m/s)**	**Bandwidth (MHz)**	**Chirp duration (μs)**
Target	All	50	20	300	25.6
Interference	Fully synchronous	250	40	300	25.6
	General synchronous			200	25.6
	Asynchronous			200	10.8

Table 5.1: Signals parameters for different CFAR detection cases

5.2.1. FULLY SYNCHRONOUS

To simulate a fully synchronous interference case, according to Table 5.1, the bandwidth and chirp duration of the interference signal is set the same as for the target signal, $B_{int} = B = 300$ MHz and $T_{int} = T = 25.6$ μs. The interference range is 250 m with a velocity of 40 m/s. Referring to Chapter 4, it is known that in the fully synchronous case, interference causes a ghost target and might have an amplitude level close to the target or even higher when the signal has low SIR. Similarly to Section 3.4, the inputs of SIR are the values before 2D-FFT.

$$SIR = \frac{s^2}{I^2} \tag{5.3}$$

where I is the level of amplitude of the interference signal.

For the example shown in Figure 5.2a, the interference power at the receiver is 10 W so that I = 20 dB. The noise power at the receiver is 56.1W transfer to amplitude is amplitude is 34.98 dB. The difference between the target and the noise level after processing is approximately 15 dB at the output of 2D-FFT. The target signal power remains at 1 W which gives the amplitude of the target at the receiver, s=0 dB. With I=20 dB and s=0 dB, according to Equation 5.3, the SIR at the input before processing (ratio between transmitted signals) is around SIR=-20 dB.

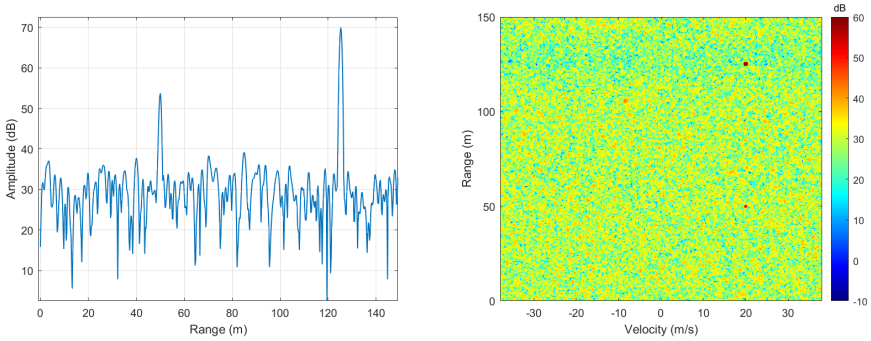

(a) (b)

Figure 5.2: 2D CFAR inputs of fully synchronous case: (a) range profile (b) range-Doppler profile

After 2D-FFT processing, there is a ghost target spike with a higher amplitude level than the real target. With P_{FA}=10^{-6}, the result of CFAR detector is represented in Figure 5.3. The cells at the location of the target (R_{target}=50 m, V_{target}=20 m/s) with red circle and the interference(R_{int}=250 m, V_{int}=40 m/s) with yellow circle are detected.

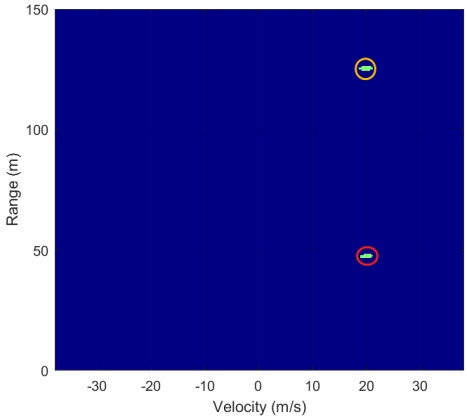

Figure 5.3: CFAR result of fully synchronous case for $P_{FA} = 10^{-6}$

To obtain the ROC curve, the input SIR of the CFAR detection algorithm is changed between -55 dB to -20 dB. Similarly to the interference-free case, five P_{FA} values, $P_{FA} = 10^{-2}, 10^{-3}, 10^{-4}, 10^{-5}$ and 10^{-6} are applied. The ROC curves of the results are shown in Figure 5.4. The results reveal that SIR and P_{FA} will not affect P_d. Here, P_d stays at 1 which means that the target is detected at all times. This is a consequence of the ghost target. The interference, instead of spreading and raising the noise floor, centralized as a spike. Thus, the surrounding cells of the target maintain a difference of 20 dB, which

will not affect CFAR setting of the threshold. As long as the noise is much lower than the target, fully synchronous interference will not degrade the detection performance. On the other hand, the ghost target can also be considered as another target. In this way, in multiple target cases, the number of targets will not influence the performance of detection, unless the targets are located too close on the range-Doppler map (less than 8 cells in range profile, 15 cells in velocity profile in this detection).

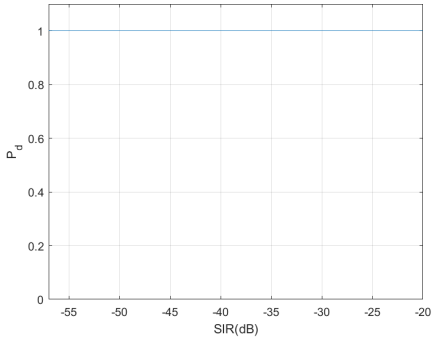

Figure 5.4: The ROC curves of fully synchronous

5.2.2. GENERAL SYNCHRONOUS

The signal parameters setting of the general synchronous interference case only changes the bandwidth of the interference signal to B_{int}=200 MHz compared to the fully synchronous case. The other parameters remain the same. According to Chapter 4, interference in the general synchronous case creates a ridge in the range domain. As shown in Figure 5.5, SIR=-20 dB at the input is given. The noise floor increases to around 45 dB and the difference in amplitude between the target and its surroundings is reduced. The input interference amplitude, in this case, is I =20 dB and the noise remains the same as in the fully synchronous case.
The corresponding result of CFAR detection for which P_{FA} =10^{-6} is applied is shown in Figure 5.6. In addition to the cells located at the target place, some cells are also detected. Those are caused by interference that increases the noise floor and with relatively high P_{FA}, some cells due to interference have higher power than the threshold.

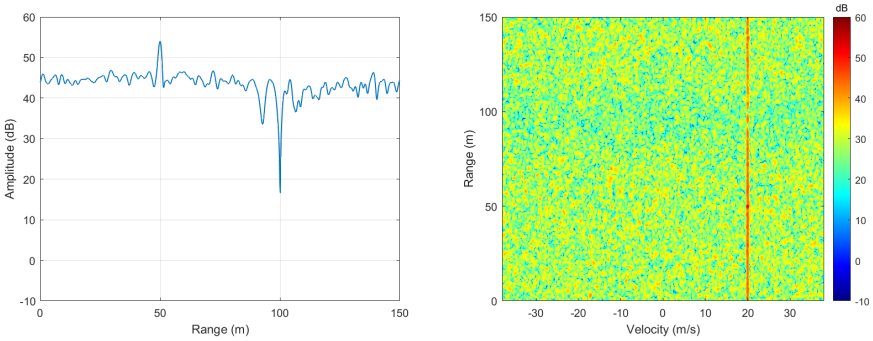

(a) (b)

Figure 5.5: 2D CFAR inputs of general synchronous case: (a) range profile (b) range-Doppler profile

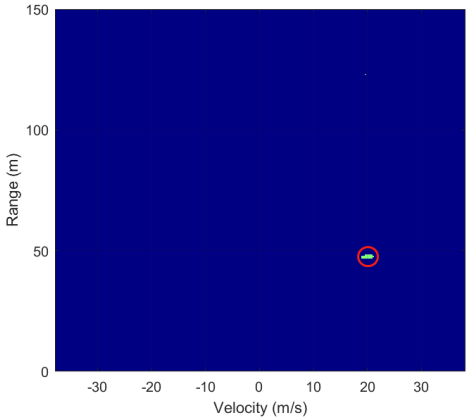

Figure 5.6: CFAR result of general synchronous case for $P_{FA} = 10^{-6}$

The entire detection setting, in this case, the same as the fully synchronous case. The result of the ROC curves is presented in Figure 5.7. It is found that P_d improves as SIR increases. Furthermore, lower P_{FA} needs better SIR to reach P_d=1. When $P_{FA} = 10^{-3}, 10^{-2}$, P_d becomes constantly 1 at all range of SIR. In comparison to no interference case given in Figure 3.9, with same noise level n= 35 dB, the required SIR should reaches -31 dB to achieve P_d=1 under P_{FA}=1e-4. When P_{FA} is higher than 10^{-3}, the general synchronous interference case seems has even higher P_d than the interference-free situation. This is because that the threshold of detector is lower than the noise floor. Consequently, in such cases, the detector may wrongly detect the noise present at the target position as an actual target, treating the noise floor as a target.

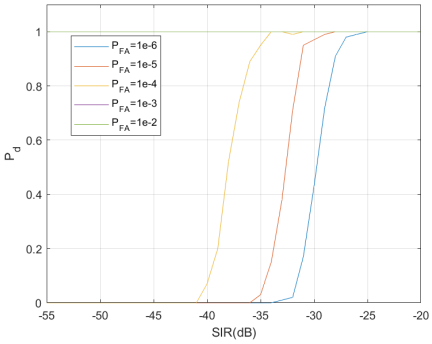

Figure 5.7: The ROC curves of general synchronous case

5.2.3. ASYNCHRONOUS

The asynchronous case here refers to the aperiodic asynchronous case in Chapter 4. As stated in Table 3.1, the chirp duration of the interference changes to T_{int}=10.8 μs. Other signal parameters stay the same as in the general synchronous case. According to Section 4.2.4, the interference spreads randomly on the rang-Doppler map. Figure 5.8 gives an example of the results of 2D-FFT in the asynchronous case with interference input amplitude I=20 dB. The interference behaves like multiples of low-power level crests spread on the range and Doppler domain.

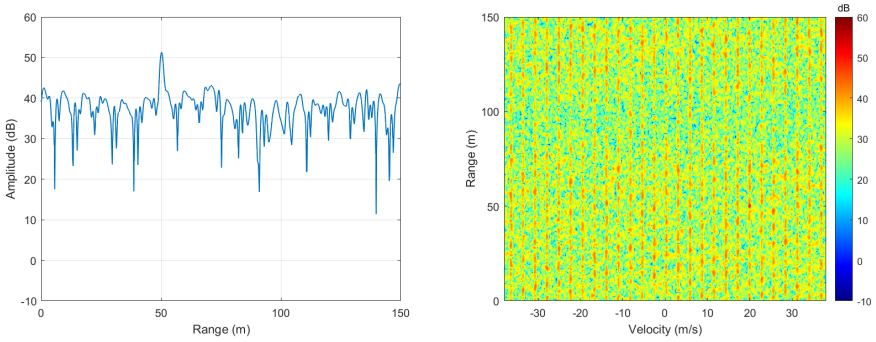

(a) (b)

Figure 5.8: 2D CFAR inputs of asynchronous case: (a) range profile (b) range-Doppler profile

Taking the range-Doppler result above as the input for the CFAR detector and applying P_{FA} =10^{-6}, the output is presented in Figure 5.9. Although the noise floor is raised to approximately 42 dB by interference (as seen at Figure 5.8a), the amplitude of the target is about 10 dB higher than the interference level. In Figure 5.9, cells located at the target location are detected and marked as 1.

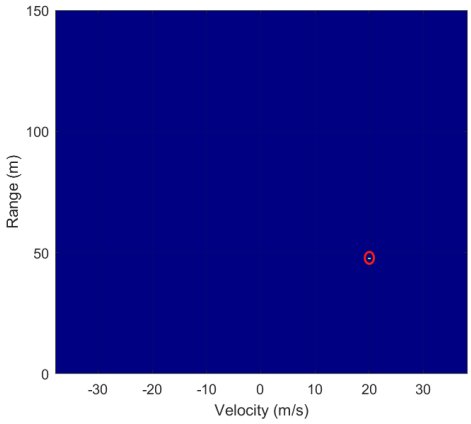

Figure 5.9: CFAR results of asynchronous case for $P_{FA} = 10^{-6}$

Similar to the synonymous case, the input SIR of the CFAR detection algorithm for the asynchronous case is changed between -55 dB to -20 dB to obtain ROC curves. For each SIR, the ROC curve is plotted by applying five different P_{FA} values. All the detection results are presented in the ROC curves in Figure 5.10. These trends of the results, the higher P_{FA} reaches $P_d = 1$ later, are in line with general synchronous. In particular, the CFAR detection reaches $P_d = 1$ around -40 dB for a P_{FA}=1e-5. In comparison to no interference case, it is observed that the value of P_d only begins to decrease when the interference amplitude level reaches 39 dB, given that the noise power is 35 dB and the desired probability of false alarm P_{FA} is set to 1e-4. Therefore, the asynchronous interference has less degradation on the target detection performance compared to synchronous case. The impact of these interference cases on the target detection will be investigated in detail in the following Section 5.2.4.

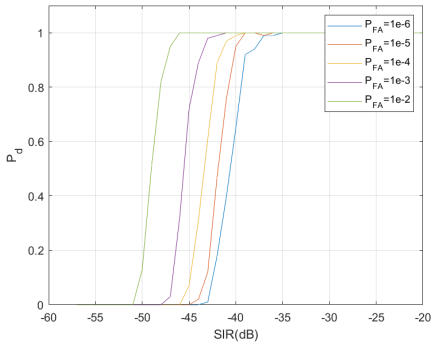

Figure 5.10: The ROC curves of asynchronous cases

5.2.4. COMPARISON BETWEEN GENERAL SYNCHRONOUS AND ASYNCHRONOUS CASE

With regards to Chapter 4, it has been observed that for both synchronous and asynchronous cases, the resulting interference after processing transforms into a noise-like floor. Consequently, the shapes of the ROC curves remain similar to the interference-free scenario, as demonstrated in Chapter 3.4. From this, it can be deduced that as the SIR after processing increases, there is an associated increase in the probability of detection.

From the ROC curves of the general synchronous and asynchronous case, it can be seen that when applying the same P_{FA} which is lower than 10^{-3}, the asynchronous case can obtain $P_d = 1$ with a lower SIR compared to the general synchronous case. For instance, when P_{FA}=10^{-5} for both cases, the asynchronous case gets $P_d = 1$ at SIR=-35 dB and the general synchronous case at SIR=-25 dB. When it is given the same interference power, for example, 40 dB, there is almost no right detection in the synchronous case compared to the asynchronous case as shown in 5.11 and 5.12 shown.

However, when P_{FA}=$10^{-3}$and 10^{-2}, the curves of P_d from general synchronous case changes to a constant 1. It seems the general synchronous interference affects less detection performance. As it is shown in Figure 5.13, when P_{FA}=10^{-3} is applied, most of the cells at velocity= 20 m/s are detected. Since the interference in the synchronous case and the asynchronous case is spread over the ridge and the plane respectively, the interference power is more centralized in the ridge than the plane. The side lobe in the synchronous case is higher than in the asynchronous case with the same interference input. In the synchronous case, the real target is covered by the noise floor caused by the interference, and the detection will not clarify whether it is the target or the interference. As long as it is detected at the reference location, it will be considered the right detection. Therefore, to reach the given P_{FA}, the threshold around the target for the synchronous case will be lower than the asynchronous case.

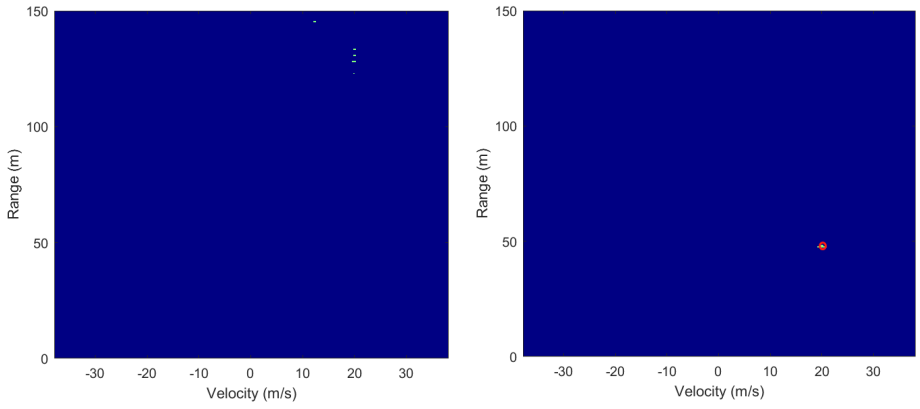

Figure 5.11: Detection results with P_{FA}=10-5 at SIR=-40 dB: (a) synchronous case (b) asynchronous case

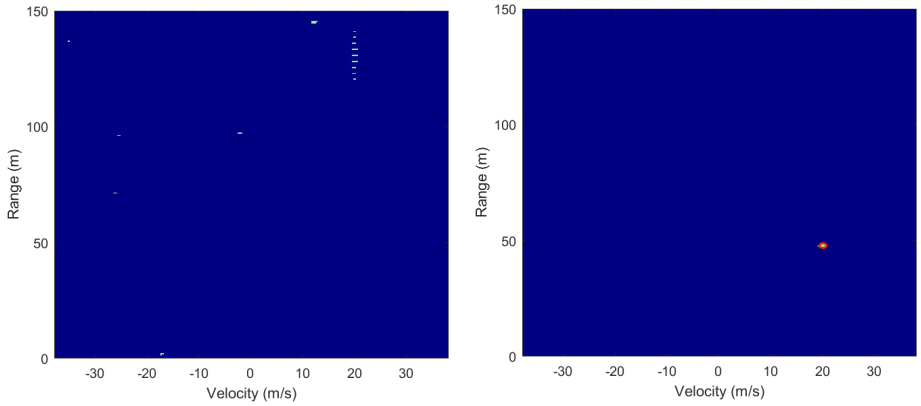

(a) (b)

Figure 5.12: Detection results with P_{FA}=10-4 at SIR=-40 dB: (a) synchronous case (b) asynchronous case

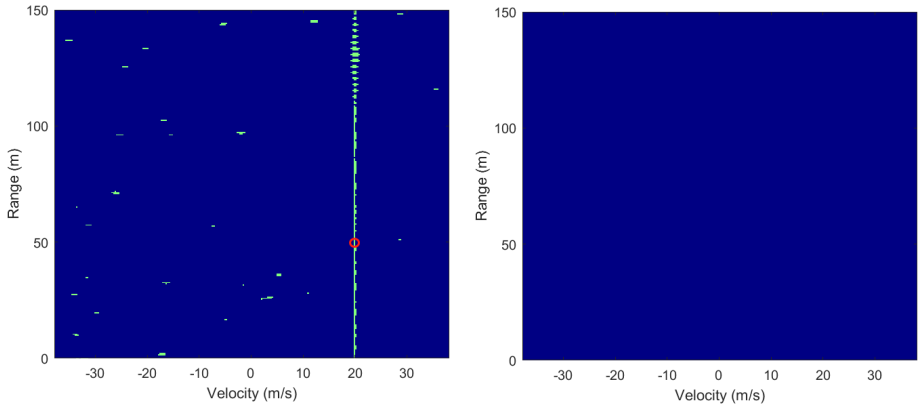

(a) (b)

Figure 5.13: Detection results with P_{FA}=10-3 at SIR=-50 dB: (a) synchronous case (b) asynchronous case

5.3. CONCLUSION

The CFAR algorithm applied in this thesis is briefly described in the first section of this chapter. To create the 2D CFAR window, the sizes of the guard band and the reference band are set to 5 and 10 cells in the range domain, 3 and 5 cells in the Doppler domain. Two hypothesis testing is considered for detection, namely H0 for the target-absent case and H1 with the target case. In Section 5.2, three cases are considered: fully synchronous,

general synchronous and asynchronous for the CFAR detection. In each case, the results of detection are presented by ROC curves.

The results of study on interference impact on target detectability can be summarized as following:

In the fully synchronous case, the interference will not spread over the range domain but will lead to a spike. It will not significantly impact the power levels of nearby cells surrounds the target cell. Thus, the change of interference power at the input would not affect P_d.

As for general synchronous interference, it will be centralized at one velocity bin as a noise floor (seen as vertical line) after processing. If the velocity of the interference is different from the target's, the interference will not affect the evaluation of the threshold. In this case, the result is similar to the interference-free case. On the other hand, if half of the velocity of the interference object is close to the target's and the interference power at the input of the receiver is high, the noise floor caused by interference will be higher than the target response. In this case, P_d can reach 1 even with low SIR when P_{FA} is high. Compared to the no interference case, to achieve a detection probability P_d= 1 with a P_{FA} of 1e-4, in the presence of interference (with a noise level of n=35 dB), the required SIR is -31 dB.

In the asynchronous case, the interference spread over the range-Doppler plane. As the level of interference power at the input increases, P_d also increases until it reaches a value of 1. In comparison to the scenario with no interference, it has been observed that P_d= 1 remains unaffected until the interference amplitude level reaches 35 dB, assuming a noise power level of 35 dB and a desired P_{FA}= 10^{-6}.

Comparing general synchronous and asynchronous cases, both general synchronous and asynchronous case, the interference after processing turns to a noise-like floor. This outcome leads to the shapes of the ROC curves being comparable to those obtained in an interference-free scenario. Thus, there exists a positive correlation between the increase in SIR after processing and the corresponding increase in the probability of detection. Besides, it is found that with the same bandwidth (B= 300 MHz and B_{int}=200 MHz), when P_{FA} is lower than or equals to 10^{-4}, asynchronous case reaches P_d=1 at SIR=-31 dB which is 8 dB lower than general synchronous case. On the other hand, when P_{FA} is higher than 10^{-4}, P_d of the synchronous case becomes 1 at very low SIR. The reason for that is the noise floor caused by interference is higher than the target in the general synchronous case with low SIR, and the detector considers the interference also as a 'target'.

6

CONCLUSION

The thesis results and contributions are summarized in this final chapter. In addition, suggestions are also given for future work.

6.1. CONCLUSIONS

This thesis is dedicated to theoretical analysis of the mutual interference of FMCW automotive radars. After reviewing the literature, it was found that there are two research gaps: 1) The mathematical expression for FMCW-to-FMCW mutual interference in the range-Doppler domain is absent; 2) Theoretical analysis of interference influence on target detectability is missing.

To better understand the behavior of the mutual interference after signal processing, the mutual interference is classified into 4 cases based on the chirp bandwidth and chirp duration: fully synchronous, general synchronous, periodic asynchronous, and aperiodic asynchronous. The analytical models of fully synchronous, general synchronous and periodic asynchronous cases are derived and validated by comparing the numerical simulation results with the quantitative simulation results of the equations giving the same parameters. Unfortunately, I was unable to derive an analytical model for the aperiodic asynchronous interference case in this thesis. Consequently, only numerical simulation results for this particular case are presented. The interference behavior was analyzed for each case.

The derivation of the analytical model in the range-Doppler domain provides convenience to researchers studying FMCW-to-FMCW mutual interference. Simulations of the various interference cases can be easily built up by entering the basic parameters to observe and analyze the interference behavior as it is shown in Chapter 4.

The other objective of this research was to examine the detection performance with FMCW mutual interference in the range-Doppler domain. This was achieved by applying the CFAR algorithm and presenting by ROC curves which include SIR, P_d and P_{FA}. In Chapter 5, the detection performance is examined with respect to three types of interference scenarios: fully synchronous, general synchronous, and asynchronous.

In addition, the detection performance analysis (ROC curves) for FMCW-to-FMCW mutual interference in different cases reveals the effect of different interference types on P_d and P_{FA} which are important factors in the application of ADAS to ensure the safety of drivers. The following conclusions for radar-to-radar interference, which have been realized by the numerical simulations, quantitative simulations and CFAR detection of Chapters 4 and 5, can be taken:

- In the **synchronous** cases, FMCW radar-to-radar mutual interference can generally be mathematically described in the range-Doppler domain. In the fully synchronous case, the interference creates a ghost target in both the range and the Doppler domain. Because of the ghost target, the probability of detection does not change significantly with different SIR. As long as the noise power after processing is lower than the ghost target spike power and the spike caused by the ghost target is not in the CFAR window of the real target in the range-Doppler domain, the CFAR detector will not change the threshold nearby the real target. This leads to P_d reaching and remaining at 1.

  In the general synchronous case, the interference spreads over the range-Doppler domain and causes a noise-like ridge in the range domain. It is coupled to the corresponding velocity profile. The processed interference amplitude level changes with the bandwidths. When the bandwidth of the interference signal approaches the bandwidth of the victim signal, the amplitude of the interference signal after processing is expected to exhibit higher levels. The processed signal's power is primarily affected by the signal processing gain, which is determined by the product of the bandwidth and chirp duration $BT$for the target response, as well as the SIR overlap factor O at the beat frequency for the interference component when a low-pass filter is applied. The level of the processed interference is linearly increased by the portion of captured interference component which is varies by different B_{int}. When B=B_{int}, the interference is fully synchronous. The detection performances, in the general synchronous case, are affected by SIR. The better SIR leads to the higher P_d (maximum 1) with the same P_{FA}. If there is a significant disparity between the velocity of the interference object and that of the target, the interference will not have a substantial impact on the determination of the threshold. In this case, the detection performance is similar to the interference-free case.

- For the **asynchronous** cases, the appearance of the periodic asynchronous interference in the range-Doppler domain can be described by the derived equations. Similarly to the general synchronous case, interference spreads in the range domain and raises the noise floor.

  The aperiodic asynchronous case is investigated only by numerical simulations. Due to the beat frequencies being different on all chirps, the interference contributions to the radar output signal are randomly spread over the range-Doppler domain. As the input interference power increases, the noise-like floor induced by processed interference also increases. Compared to synchronous cases, the interference in aperiodic cases spreads over the range-Doppler plane rather than a ridge. This leads to the aperiodic interference having a lower power level than the

other cases on the range-Doppler map after processing with the same input interference power level. The SIR is determined by the power at the receiver, the processing gain, O and the coherent Doppler processing gain.

- Except for the fully synchronous case, the detection performances are affected by SNR or SIR. It has been observed that in both synchronous and asynchronous scenarios, the interference present after processing is transformed into a noise floor. This outcome leads to the ROC curves' shapes being similar to those obtained in an interference-free scenario. The better SNR or SIR leads to the higher P_d (maximum 1). Moreover, the lower desired P_{FA} setting leads to the lower power threshold of detection. It means that targets can be reliable detected (P_d=1) with a lower values of SNR or SIR than in the fully synchronous case. With the same and relatively low P_{FA}, the asynchronous case can obtain P_d=1 with a lower SIR compared to the general synchronous case. When P_{FA} becomes higher, the noise floor caused by the general synchronous interference might be considered as a "target" when the level of the noise floor is close to the target's. In this case, the detection in the general synchronous case can reach P_d=1 easier than the detection in the asynchronous case.

6.2. RECOMMENDATIONS

The following recommendations are provided to improve the knowledge of mutual interference between automotive radars:

- During the derivation of equations for FMCW interference, in this thesis the mathematical model of fully asynchronous cases could not be obtained. In practice, this situation is common for different cars sending various signals with different chirp duration. Thus, if full asynchronous equations are generated, then it will enable people to better understand mutual interference numerically.
- With the application of PC-FMCW in the automotive industry, more research is needed on mutual interference between PC-FMCW and FMCW radars or between PC-FMCW and PC-FMCW radars. Since the frequency-modulated component of the PC-FMCW radar signal is the same as the FMCW signal, the mathematical model of this thesis has a high probability that can be applied to interference research on PC-FMCW. And this remains to be examined.
- Due to the lack of computational ability and time constraints, instead of $\frac{100}{P_{FA}}$, only 100 CFAR detection repetitions are taken for each circumstance in the detection performance analysis. A larger number of detection times is required to achieve more accurate numerical relationships between SIR, detected probability, and false alarm rate.

REFERENCES

[1] S. M. Patole, M. Torlak, D. Wang, and M. Ali, "Automotive radars: A review of signal processing techniques," *IEEE Signal Processing Magazine*, vol. 34, no. 2, pp. 22–35, 2017.

[2] V. Shrivathsa, "Cell averaging-constant false alarm rate detection in radar," *International Research Journal of Engineering and Technology (IRJET)*, vol. 7, pp. 2433–2438, 2018.

[3] H. H. Meinel, "Evolving automotive radar — from the very beginnings into the future," in *The 8th European Conference on Antennas and Propagation (EuCAP 2014)*, 2014, pp. 3107–3114.

[4] F. Roos, J. Bechter, C. Knill, B. Schweizer, and C. Waldschmidt, "Radar sensors for autonomous driving: Modulation schemes and interference mitigation," *IEEE Microwave Magazine*, vol. 20, no. 9, pp. 58–72, 2019.

[5] R. Aufrère, J. Gowdy, C. Mertz, C. Thorpe, C.-C. Wang, and T. Yata, "Perception for collision avoidance and autonomous driving," *Mechatronics*, vol. 13, no. 10, pp. 1149–1161, 2003, mechatronics - a 12 year celebration. [Online]. Available: https://www.sciencedirect.com/science/article/pii/S0957415803000473

[6] H. Chen, F. Zhao, K. Huang, and Y. Tian, "Driver behavior analysis for advanced driver assistance system," in *2018 IEEE 7th Data Driven Control and Learning Systems Conference (DDCLS)*, 2018, pp. 492–497.

[7] F. Roos, J. Bechter, C. Knill, B. Schweizer, and C. Waldschmidt, "Radar sensors for autonomous driving: Modulation schemes and interference mitigation," *IEEE Microwave Magazine*, vol. 20, no. 9, pp. 58–72, 2019.

[8] U. Kumbul, N. Petrov, F. van der Zwan, C. S. Vaucher, and A. Yarovoy, "Experimental investigation of phase coded fmcw for sensing and communications," in *2021 15th European Conference on Antennas and Propagation (EuCAP)*, 2021, pp. 1–5.

[9] U. Kumbul, N. Petrov, C. S. Vaucher, and A. Yarovoy, "Receiver structures for phase modulated fmcw radars," in *2022 16th European Conference on Antennas and Propagation (EuCAP)*, 2022, pp. 1–5.

[10] U. Kumbul, F. Uysal, C. S. Vaucher, and A. Yarovoy, "Automotive radar interference study for different radar waveform types," *IET Radar, Sonar & Navigation*, vol. 16, no. 3, pp. 564–577, 2022. [Online]. Available: https://ietresearch.onlinelibrary.wiley.com/doi/abs/10.1049/rsn2.12203

[11] U. Kumbul, N. Petrov, C. S. Vaucher, and A. Yarovoy, "Sensing performance of different codes for phase-coded fmcw radars," in *2022 19th European Radar Conference (EuRAD)*, 2022, pp. 1–4.

[12] U. Kumbul, N. Petrov, C. S. Vaucher, and A. Yarovoy, "Smoothed phase-coded fmcw: Waveform properties and transceiver architecture," *IEEE Transactions on Aerospace and Electronic Systems*, pp. 1–18, 2022, doi:10.1109/TAES.2022.3206173.

[13] U. Kumbul, N. Petrov, S. Yuan, C. S. Vaucher, and A. Yarovoy, "Mimo ambiguity functions of different codes with application to phase-coded fmcw radars," in *IET International Radar Conference (IET IRC 2022)*, 2022, pp. 1–6.

[14] U. Kumbul, N. Petrov, C. S. Vaucher, and A. Yarovoy, "Phase-coded fmcw for coherent MIMO radar," *IEEE Transactions on Microwave Theory and Techniques*, pp. 1–13, 2022, doi:10.1109/TMTT.2022.3228950.

[15] I. Bilik, O. Longman, S. Villeval, and J. Tabrikian, "The rise of radar for autonomous vehicles: Signal processing solutions and future research directions," *IEEE Signal Processing Magazine*, vol. 36, no. 5, pp. 20–31, 2019.

[16] S. Alland, W. Stark, M. Ali, and M. Hegde, "Interference in automotive radar systems: Characteristics, mitigation techniques, and current and future research," *IEEE Signal Processing Magazine*, vol. 36, no. 5, 2019.

[17] C. Aydogdu, M. F. Keskin, G. K. Carvajal, O. Eriksson, H. Hellsten, H. Herbertsson, E. Nilsson, M. Rydstrom, K. Vanas, and H. Wymeersch, "Radar interference mitigation for automated driving: Exploring proactive strategies," *IEEE Signal Processing Magazine*, vol. 37, no. 4, pp. 72–84, 2020.

[18] S. M. Patole, M. Torlak, D. Wang, and M. Ali, "Automotive radars: A review of signal processing techniques," *IEEE Signal Processing Magazine*, vol. 34, no. 2, pp. 22–35, 2017.

[19] M. Kunert, H. Meinel, C. Fischer, and M. Ahrholdt, "Report on interference density increase by market penetration forecast," in *MOSARIM Consortium, CNTR, Tech. Rep. D1.6, Sep.*, 2010.

[20] G. M. Brooker, "Mutual interference of millimeter-wave radar systems," *IEEE Transactions on Electromagnetic Compatibility*, vol. 49, no. 1, pp. 170–181, 2007.

[21] T. Schipper, S. Prophet, M. Harter, L. Zwirello, and T. Zwick, "Simulative prediction of the interference potential between radars in common road scenarios," *IEEE Transactions on Electromagnetic Compatibility*, vol. 57, no. 3, pp. 322–328, 2015.

[22] A. Pirkani, F. Norouzian, E. Hoare, M. Cherniakov, and M. Gashinova, "Automotive interference statistics and their effect on radar detector," *IET Radar, Sonar & Navigation*, vol. 16, no. 1, pp. 9–21, 2022.

[23] C. Aydogdu, M. F. Keskin, G. K. Carvajal, O. Eriksson, H. Hellsten, H. Herbertsson, E. Nilsson, M. Rydstrom, K. Vanas, and H. Wymeersch, "Radar interference mitigation for automated driving: Exploring proactive strategies," *IEEE Signal Processing Magazine*, vol. 37, no. 4, pp. 72–84, 2020.

[24] Z. Tong, R. Renter, and M. Fujimoto, "Fast chirp fmcw radar in automotive applications," in *IET International Radar Conference 2015*, 2015, pp. 1–4.

[25] K. Fuller, "Avoid–short range high definition radar," *Wireless World*, vol. 76, no. 1425, pp. 110–113, 1971.

[26] R. Lindop, "A fast fourier transform processor using shift registers," *Mullard Research Laboratories An. Rev.*, pp. 42–45, 1975.

[27] I. Komarov and S. Smolskiy, 2003.

[28] H. Kwon and B. Kang, "Linear frequency modulation of voltage-controlled oscillator using delay-line feedback," *IEEE Microwave and Wireless Components Letters*, vol. 15, no. 6, pp. 431–433, 2005.

[29] C. Cao and K. O, "Millimeter-wave voltage-controlled oscillators in 0.13-/spl mu/m cmos technology," *IEEE Journal of Solid-State Circuits*, vol. 41, no. 6, pp. 1297–1304, 2006.

[30] W. Winkler, J. Borngraber, and B. Heinemann, "Lc-oscillators above 100 ghz in silicon-based technology," in *Proceedings of the 30th European Solid-State Circuits Conference*, 2004, pp. 131–134.

[31] A. Bourdoux, K. Parashar, and M. Bauduin, "Phenomenology of mutual interference of fmcw and pmcw automotive radars," in *2017 IEEE Radar Conference (RadarConf)*, 2017, pp. 1709–1714.

[32] G. V. Weinberg, "On the construction of cfar decision rules via transformations," *IEEE Transactions on Geoscience and Remote Sensing*, vol. 55, no. 2, pp. 1140–1146, 2016.

[33] M. Barkat, *Signal detection and estimation*. Artech House Publishers, 2005.

[34] K. Tan, T. Yin, H. Ruan, S. Balon, and X. Chen, "Learning approach to fmcw radar target classification with feature extraction from wave physics," *IEEE Transactions on Antennas and Propagation*, vol. 70, no. 8, pp. 6287–6299, 2022.

[35] X. Cai and K. Sarabandi, "A machine learning based 77 ghz radar target classification for autonomous vehicles," in *2019 IEEE International Symposium on Antennas and Propagation and USNC-URSI Radio Science Meeting*, 2019, pp. 371–372.

[36] M. A. Richards, *Fundamentals of Radar Signal Processing*. US: McGraw-Hill, 2005.

[37] M. I. Skolnik, *Radar handbook*. McGraw-Hill Education, 2008.

[38] A. Bourdoux, K. Parashar, and M. Bauduin, "Phenomenology of mutual interference of fmcw and pmcw automotive radars," in *2017 IEEE Radar Conference (RadarConf)*, 2017, pp. 1709–1714.

[39] H. Rohling and R. Mende, "Os cfar performance in a 77 ghz radar sensor for car application," in *Proceedings of International Radar Conference*, 1996, pp. 109–114.

[40] W. Zhou, J. Xie, K. Xi, and Y. Du, "Modified cell averaging cfar detector based on grubbs criterion in non-homogeneous background," *IET Radar, Sonar & Navigation*, vol. 13, no. 1, pp. 104–112, 2019.

[41] H. M. Finn, "Adaptive detection mode with threshold control as a function of spatially sampled clutter-level estimates," *Rca Rev.*, vol. 29, pp. 414–465, 1968.

[42] M. A. Richards, *Fundamentals of Radar Signal Processing*. McGraw Hill, 2022.

[43] A. A. Belyaev, I. O. Frolov, T. A. Suanov, and D. O. Trots, "Object detection in an urban environment using 77ghz radar," in *2019 Radiation and Scattering of Electromagnetic Waves (RSEMW)*. IEEE, 2019, pp. 436–439.